

VILNIUS UNIVERSITY  
CENTER FOR PHYSICAL SCIENCES AND TECHNOLOGY

LINAS MINKEVIČIUS

TERAHERTZ IMAGING ARRAYS FOR ROOM TEMPERATURE OPERATION

Summary of doctoral thesis  
Physical Sciences, Physics (02 P)

Vilnius, 2016

The research has been carried out in 2011 – 2016 at the Center for Physical Sciences and Technology.

Scientific supervisor – prof. dr. Vincas Tamošiūnas (Center for Physical Sciences and Technology and Vilnius University, Physical sciences, Physics – 02 P).

Dissertation will be defended in united Vilnius University and Center for Physical Sciences and Technology council of physical sciences:

Chairman – prof. habil. dr. Gintautas Tamulaitis (Vilnius University, Physical sciences, Physics – 02 P).

Members:

dr. Ramūnas Adomavičius (Center for Physical Sciences and Technology, Physical sciences, Physics – 02 P);

prof. habil. dr. Saulius Antanas Juršėnas (Vilnius University, Physical sciences, Physics – 02 P);

prof. habil. dr. Jerzy Łusakowski (University of Warsaw, Physical sciences, Physics – 02 P);

prof. habil. dr. Sigitas Tamulevičius (Kaunas University of Technology, Physical sciences, Physics – 02 P).

The dissertation will be defended under open consideration in the council of physics on 20 th June, 2016, 10 a.m. at the Center for Physical Science and Technology, seminar room (room D401).

Address: Saulėtekio av. 3, Vilnius, Lithuania.

The summary of the dissertation was distributed on May 20, 2016.

The dissertation is available in Vilnius University, Center for Physical Science and Technology libraries and in VU web site: [www.vu.lt/lt/naujienos/ivykiu-kalendorius](http://www.vu.lt/lt/naujienos/ivykiu-kalendorius).

VILNIAUS UNIVERSITETAS  
FIZINIŲ IR TECHNOLOGIJOS MOKSLŲ CENTRAS

LINAS MINKEVIČIUS

TERAHERCINIŲ VAIZDŲ UŽRAŠYMO MATRICOS, VEIKIANČIOS KAMBARIO  
TEMPERATŪROJE

Daktaro disertacijos santrauka  
Fiziniai mokslai, fizika (02 P)

Vilnius, 2016

Disertacija rengta 2011 – 2016 metais Fizinių ir technologijos mokslų centre.

Mokslinis vadovas – prof. dr. Vincas Tamošiūnas (Fizinių ir technologijos mokslų centras ir Vilniaus universitetas, fiziniai mokslai, fizika – 02 P).

Disertacija ginama Vilniaus universiteto ir Fizinių ir technologijos mokslų centro jungtinėje Fizikos mokslo krypties taryboje:

Pirmininkas – prof. habil. dr. Gintautas Tamulaitis (Vilniaus universitetas, fiziniai mokslai, fizika – 02 P).

Nariai:

dr. Ramūnas Adomavičius (Fizinių ir technologijos mokslų centras, fiziniai mokslai, fizika – 02 P);

prof. habil. dr. Saulius Antanas Juršėnas (Vilniaus universitetas, fiziniai mokslai, fizika – 02 P);

prof. habil. dr. Jerzy Łusakowski (Varšuvos universitetas, fiziniai mokslai, fizika – 02P);

prof. habil. dr. Sigitas Tamulevičius (Kauno technologijos universitetas, fiziniai mokslai, fizika – 02 P).

Disertacija bus ginama viešame Fizikos mokslo krypties tarybos posėdyje 2016 birželio 20 d. 10 val. Fizinių ir technologijos mokslų centre, seminarų salėje (D401 kab.).

Adresas: Saulėtekio al. 3, Vilnius, Lietuva.

Disertacijos santrauka išsiuntinėta 2016 m. gegužės mėn. 20 d.

Disertaciją galima peržiūrėti Vilniaus universiteto, Fizinių ir technologijos mokslų centro bibliotekose ir VU interneto svetainėje adresu: [www.vu.lt/lt/naujienos/ivykiu-kalendorius](http://www.vu.lt/lt/naujienos/ivykiu-kalendorius).

## Santrauka

Terahercine spinduliuote dažniausiai vadinamos elektromagnetinės bangos, kurių dažniai yra tarp 100 GHz ir 10 THz ( $1 \text{ THz} = 10^{12} \text{ Hz}$ ), arba bangos ilgiai tarp 3 mm ir 30  $\mu\text{m}$ . Skirtingai nei rentgeno spinduliuotė, terahercinės bangos neturi jokio jonizuojančio poveikio ir paprastai yra laikomos biologiškai nekenksmingomis. Dėl to šis medžiagos neardantis tyrimų būdas yra vis plačiau taikomas praktikoje.

Pagrindinis šios disertacijos tikslas buvo sukurti optimizuotus peteliškės tipo InGaAs jutiklius teraherciniam dažnių ruožui, tinkančius jutiklių matricoms kompaktiškose kambario temperatūroje veikiančiose vaizdinimo sistemose, surasti difrakcinės optikos sprendimus, galinčius pagerinti sistemos parametrus bei ištirti tokių jutiklių, jų matricų ir kompaktiškų vaizdinimo sistemų taikymo galimybes.

Disertaciją sudaro įvadinė dalis, šeši skyriai ir išvados. Įvade trumpai pristatoma terahercų dažnių spinduliuotės specifika bei pagrindinės darbo idėjos. Paaiškinama darbo motyvacija, iškelti uždaviniai, praktinė vertė ir naujumas. Taip pat pristatomi ginamieji teiginiai, autoriaus indėlis ir paskelbtų darbų sąrašas. Pirmajame skyriuje apžvelgiamos terahercinės vaizdinimo sistemos ir jose naudojami jutikliai. Kiek plačiau aprašoma „peteliškės“ formos jutiklio sukūrimo istorija ir jo taikymai terahercinio vaizdinimo eksperimentuose. Trumpai apžvelgiama literatūra susijusi su difrakcinės optikos ir dažniui selektyvių paviršių taikymais terahercinės spinduliuotės fokusavimui. Antrajame skyriuje aptariami elektrinių laukų pasiskirstymo modeliavimo rezultatai naujo dizaino InGaAs jutikliuose. Trečiajame skyriuje aprašoma jutiklio gamybos technologija ir jų charakterizavimas bei aptariamas jutiklio veikimo modelio papildymas. Ketvirtasis skyrius yra skirtas jutiklio savybių tyrimams tiesioginės ir heterodininės detekcijos schemose. Taip pat šiame skyriuje pristatomos jutiklių liniuotės ir vaizdinimas su jomis. Difrakcinių elementų tyrimai, jų taikymai terahercinės spinduliuotės fokusavimui bei galimybės juos integruoti jutiklių masyvuose aptariamos penktajame skyriuje. Šeštajame skyriuje aptariami terahercinės spinduliuotės taikymai saulės elementų kokybės kontrolėje. Pristatomos sukurtų jutiklių liniuočių taikymo idėjos sparčiose saulės elementų gamybos linijose.

## **Acknowledgement**

I would like to give my special thanks to my scientific supervisor prof. dr. Vincas Tamošiūnas for expressed trust, care and inspiration during many years of collaboration.

I would like to say special thanks prof. habil. dr. Gintaras Valušis for scientific discussions, the expressed scientific ideas for my thesis and for a possibility to do research work in the Center for Physical Science and Technology.

Also I wish to thank dr. Irmantas Kašalynas and Rimvydas Venckevičius for their support in the experimental measurements. I sincerely grateful for the whole Terahertz Photonics Laboratory for scientific discussions.

I acknowledge dr. Bogdan Voisiat (Center for Physical Science and technology) for diffractive optics components production, and Noise laboratory (Faculty of Physics, Vilnius University) for noise measurements. I also thank dr. Alvydas Lisauskas (Johann Wolfgang Goethe University, Germany) for help and advice during direct and heterodyne imaging experiments, Bernhard Klug (Johann Wolfgang Goethe University, Germany) for assistance during sample lithography process, Klaus Köhler (Fraunhofer-Institut für Angewandte Festkörperphysik, Germany), Renata Butkutė, Virginijus Bukauskas (Physical Science and technology center) for InGaAs wafers fabrication and characterization.

Finally, I would like to thank my parents, brother, my wife Monika and son Benediktas for support, encouragement and patience.

# INTRODUCTION

Terahertz radiation range is between electromagnetic wave spectra from 100 GHz and 10 THz ( $1 \text{ THz} = 10^{12} \text{ Hz}$ ) or wavelength from 3 mm to  $30 \mu\text{m}$  [1]. This radiation has a feature to penetrate through dielectric, textile, plastic, paper and other materials. It can be used as a nondestructive way to inspect objects in customs and airports [2]; to locate the defects in solar cells panels [IP 5] and even as an auxiliary way in cancer diagnostics in medicine [3].

All of these applications require different terahertz imaging systems solutions. Particular attention goes to fast sensors and sensor technologies which have the potential for real-time imaging while maintaining a high dynamic range. Furthermore, it is highly desirable to be able to operate the devices at room temperature (RT). Examples of sensors fulfilling these requirements are: Schottky detectors [4], microbolometers arrays [5,6] and semiconductor field-effect transistors (FETs) [7]. An important role during the development of imaging systems goes to simplicity and reliability of THz detectors. Planar asymmetrically shaped – also called bow-tie (BT) diodes because of their general shape should be mentioned. Asymmetric shape GaAs/AlGaAs sensors are robust and electrostatic resistant. However, direct application of such detectors in THz imaging systems are difficult due to their low sensitivity at room temperature [8].

Several steps should be done in order to increase the detector sensitivity. First, alternative materials could be employed, such as InGaAs due to its high electrons mobility at room temperature [9]. Also, the design of the sensor antenna should be considered. Moreover, detector ability to operate in heterodyne mode [10] could increase the dynamic range of imaging systems. Finally, modern compact diffractive optics components, suitable for detector arrays should be considered. To complete all above-mentioned processes, complex interaction studies of sensors and diffractive focusing elements should be performed.

Thus, resolving these challenges, widely used relative slow spectroscopic imaging systems in future could be changed with much faster system consisting of sensors array, working in heterodyne mode. Such solutions can find the applications in material inspection or solar cells quality control in fast production line.

## **Main goal and objectives**

The aim of this dissertation was to create optimized for THz range compact arrays of InGaAs bow-tie type sensors and to explore the possibilities of their applications.

### **In order to reach this goal, main objectives were defined:**

- To optimize bow-tie shaped InGaAs sensor design for THz frequency range by taking into account simulation results of antenna effects in separate metallic parts of the detector.
- To produce optimized bow-tie shaped terahertz InGaAs sensors and their arrays, operating at room temperature, by modern semiconductor processing technologies.
- To evaluate sensitivity and noise parameters of produced InGaAs bow-tie sensors when used for direct and heterodyne detection. Investigate applications of these sensors arrays in THz imaging systems. Supplement their operation model by evaluating and including the possible influence of surface charge and resistive self-mixing effect.
- To create designs of thin terahertz zone plates and combined diffractive optics and simulate numerically their performance. To evaluate both theoretically and experimentally their focusing properties in THz frequency range.
- To integrate the zone plate on the substrate of bow-tie sensor in order to reduce the dimensions of imaging systems and investigate their interaction.
- To investigate the practical possibilities of terahertz radiation applications to localize various solar cell and module defects in quality control systems of modern fast photovoltaic production lines.

### **Novelty**

- Using Finite Differences Time domain method, the changes of electric field at the apex of active part influence were simulated by varying sensors' metallic part length and tapering angle. Depending on the simulated different metallic area resonances, new optimum InGaAs bow-tie shape designs for THz frequency range were created. These results also lead to an updated phenomenological sensitivity model better matching with experimental results.
- Results obtained by means of Kelvin probe force, scanning tunneling microscopy measurements and Synopsys TCAD semiconductors simulations were interpreted for



high resistivity ( $>50 \text{ k}\Omega/\text{sq}$  sheet resistance) detectors. Investigation confirmed, that field-effect induced conductivity modulation is a possible contributing mechanism to high sensitivity of these detectors.

- For the first time, InGaAs bow-tie detector performance in direct and heterodyne modes was compared. The detector sensitivity was estimated to reach  $6 \text{ V/W}$  at direct detection mode and imaging system dynamic range enhancement of  $43 \text{ dB}$  was observed in heterodyne mode.
- For the first time, bow-tie sensor arrays with integrated low noise amplifiers have been demonstrated, leading to the possibility to shorten THz imaging time up to 32 times compared to a single detector system.
- The zone plate integration idea on the bow-tie device substrate was presented and successfully employed for the first time. Its influence to bow-tie sensors response signal was confirmed by theoretical simulations. Experimental studies have demonstrated that this solution can increase the sensors signal amplitude more than 20 times.
- Multiple terahertz imaging applications for solar cells and modules were demonstrated. Detection of soldering defects, ability to monitor the quality of the anisotropic etching of silicon and detection of defects in the protective layers of the solar cell module were demonstrated.

### **The practical value of the thesis**

1. Created InGaAs sensors array with developed low noise amplifiers could be used for fast signal read out in compact THz imaging systems, capable to operate at ambient environmental conditions.
2. The application of compact THz zone plate could increase the resolution of imaging system up to 25 % in comparison with bulkier parabolic mirror of the same numerical aperture.
3. The zone plate integration in the substrate of BT sensor increases the detector response amplitude and, at the same time, simplifies the imaging system for increased practical applications possibilities.
4. It was demonstrated, that THz radiation is suitable not only for traditional applications such as inspection of hidden objects, but also for photovoltaic industry

production lines for tab wire soldering defect identification on silicon solar cells, etching control of antireflective surfaces or for accurate homogeneity evaluation of solar module encapsulation materials.

### **Statements to defend**

1. The electric field amplitude at the apex of antenna has the greatest impact for the experimentally observed bow-tie shaped InGaAs detector sensitivity reduction above 1 THz; moreover, the sensor metalized areas act as two separate antennas with their own resonances.
2. The shape of current-voltage characteristics and changes of the detected signal due to bias current of bow-tie InGaAs sensors, made of InGaAs layer of more than 50 k $\Omega$ /sq sheet resistance are caused by field effect due to surface charges.
3. System dynamic range improvement above 40 dB in comparison to direct detection scheme can be reached due to reduction of noise influence using optimized bow-tie shaped InGaAs sensors in the heterodyne detection scheme.
4. InGaAs sensor arrays are suitable for independent readout of detected signals at the frequencies above 0.5 THz due to low influence of adjacent sensors if a period between sensors is at least 135  $\mu$ m.
5. Modified zone plates for THz range and combined zone plates are suitable for sharp THz beam focusing. Bow-tie shaped InGaAs sensor signal enhancement of more than 20 times and reduction of bulky optical components number in the system are obtained with on-chip integrated zone plates.

### **Contribution of the author**

The author has carried out all the theoretical simulations using the Finite-Difference Time-Domain method, when investigating antenna-related effects of the sensor and designs of the zone plates. Also, the author carried out all the work related to the production of the sensors ranging from mask patterning to detector encapsulation. Detectors were fabricated during summer practice in the Physics Institute of the Johann Wolfgang Goethe University, Germany. The author also performed the InGaAs sensors characterization, imaging experiments, focusing experiments of diffractive optics and terahertz radiation applications experiments for the solar cell diagnostics. The author has prepared initial versions of the manuscripts of an articles related to the topic of the thesis,

also participated in the preparation of reports for conferences, some of them introduced by himself. InGaAs epilayers were grown by dr. Renata Butkutė (CPST, Optoelectronics department) and Klaus Köhler (Fraunhofer Institute for Applied Solid State Physics, Germany). Measurement by transmission electron microscopy was made by dr. Rokas Kondrotas (CPST, Department of Characterization of Materials Structure). Sensor noise results were obtained in collaboration with Noise Research Laboratory (Vilnius University, Faculty of Radiophysics Department). Electrostatic potential distribution calculations with Sypapsys TCAD package were made by dr. Ernestas Žašinas (Vilnius University, Faculty of Physics, Semiconductor Physics Department). Measurements by atomic force microscopy were performed by dr. Virginijus Bukauskas (CPST, Department of Physical Technologies). Compact diffractive optics components were ablated by dr. Bogdan Voisiat (CPST, Laser technology department).

Supervision of students K. Madeikis and M. Šoliūnas in the project “Promotion of students Scientific Activities”.

# 1 BOW-TIE InGaAs-BASED TERAHERTZ SENSORS

Compact room temperature operating systems, able to register terahertz radiation, research and development continues to be one of the key challenges in the THz frequency range [11,12]. Requirements for the sensors in real-time imaging systems are: wide dynamic range; operation at room temperature; possibility to make detector arrays; preference to planar-technology-based solutions.

While searching for a durable and technologically simple solution, asymmetrically shaped  $n-n^+$  GaAs THz sensor, presented at 2003 [8], should be considered. These type of sensors are resistant to electrostatic charge and do not change its properties, even illuminated by a constant 1 W electromagnetic radiation power. They have wide dynamic range and sensitivity at room temperature reaches about 0.3 V/W at frequency range from 30 GHz to 700 GHz range [13]. At 2004, novel approach to detect terahertz radiation was proposed by authors [14]. They suggested to use an asymmetrically-shaped diode containing a 2DEG layer based on a modulation doped GaAs/AlGaAs structure. Principle of operation is based on incident radiation coupling into the 2DEG layer. As a result, the 2DEG is heated non-uniformly, thus a voltage signal over the ends of the device is induced.

Due to low sensitivity at room temperature, these detectors are difficult to apply in practical applications. Authors [15] at 2006 suggested to use material with a larger electron mobility by switching from GaAs to  $\text{In}_{0.54}\text{Ga}_{0.46}\text{As}$  as the active layer material and coupling the processed structures with a hemispherical silicon lens (Fig. 1 a).

The device exhibits a voltage sensitivity of around 5 V/W below 1 THz (Fig. 1 b), and it is suited for sensing over a broad frequency band, from 10 GHz to 2.5 THz, in a passive detection scheme at room temperature [16,17].

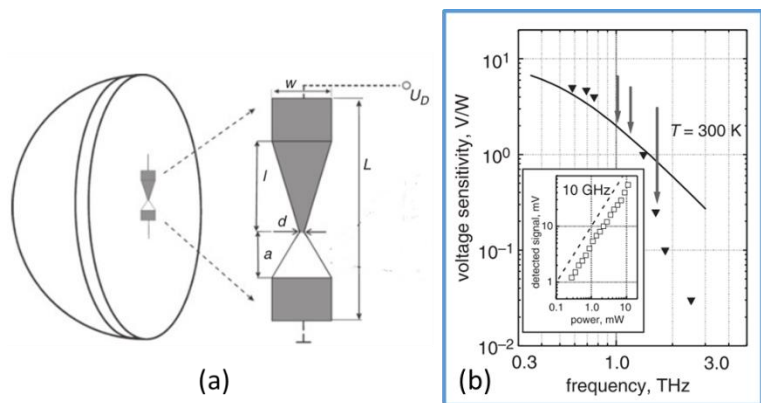


Fig. 1. Schematic view of the bow-tie diode shape and silicon lens (a). Voltage sensitivity against frequency at 300 K (b) [15].

## 2 BOW-TIE DETECTOR ANTENNA EFFECTS SIMULATION

Bow-tie detectors sensitivity at frequencies above 1 THz is low due to a weak radiation coupling into active part. It was suspected, that this may be caused by antenna effects and different resonances of separate metallic detector areas.

Distribution of the electromagnetic fields in the space of semiconductor of the THz detector was simulated by three-dimensional (3D) finite-difference time-domain (FDTD) method [18]. Characteristic design of the bow-tie detector is shown schematically in Fig.2 a. In turn to explore how

different parts of the antenna effect an electric field distribution in the sensor, simulations for alternately changed metallization areas in the sensor were made (Fig. 2 b). As one can see, all peaks from the 1st spectrum (blue line) and the 3rd spectrum (green dotted line) have the same frequency, but the amplitude is smaller for the case

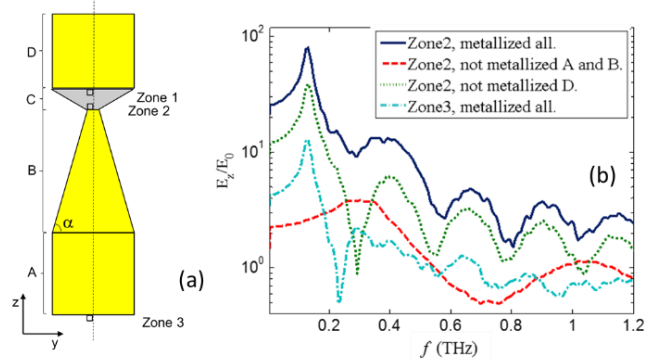


Fig. 2. Schematic view of the device (not to scale) (a). Electrical field amplitude  $E_z$  ratio with incident wave amplitude  $E_0$  dependence on frequency when the metallization parts were changed (b) [IP 7].

when D part is not metallized (green dotted line). This effect appears because the electric field is not concentrated in a small area between metallized surfaces. Electric field spectrum when just D part is metallized (red dashed line) explains why in the case of full metallization the electric field decrease between the first and the second peaks in the 1st spectrum is not observed (deep minimum at 0.3 THz, as it appears in the 3rd spectrum). Its first amplitude maxima at 0.25 – 0.3 THz (dashed line) compensates the minimum caused by A and B parts, helping to maintain the electric field amplitude between the metal contacts [IP 7].

### 2.1 Comparison of theoretical and experimental results

Previous experimental studies have demonstrated that the detector sensitivity decreases with frequency more rapidly than can be expected from the phenomenological model [15].

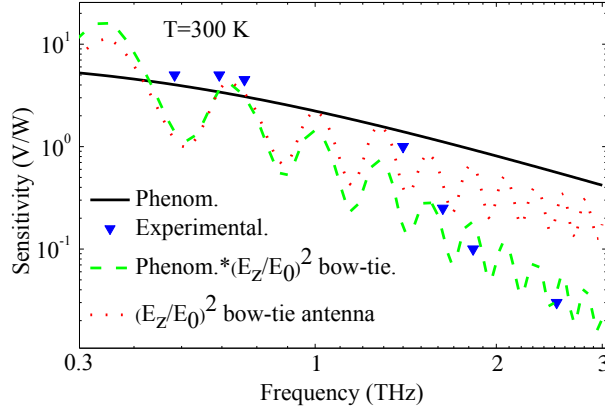


Fig. 3. Sensitivity dependence of the InGaAs bow-tie diode on frequency in THz frequency region. Phenomenological calculation [8] was marked black line. Experimental data [15] were marked as triangle symbols. Simulated bow - tie sensitivity dependence on frequency, in which corrected phenomenological model and bow tie detector simulation results were evaluated, is depicted by green dashed line. Simulated  $(E_z/E_0)^2$  distribution dependence on frequency is shown by dotted line [IP 7].

overlap is made, the full range of sensitivity between the resonance peaks and the “bottoms of holes” should be taken into account, because the attached contact wires could influence precise positions of resonance maxima during the experiment.

Finally, it deserves to indicate that the antenna/coupling related effects could be responsible for the deviations from the monotonical frequency dependence of the sensitivity within 1 – 2 THz range [IP 7].

## 2.2 Simulation of sensors operation in dense array

The investigation of frequency dependent properties [IP 7] of the BT diodes revealed that the sensitivity enhancement can be expected if dimensions of tapered metallic part of the BT diode are comparable with quarter wavelength in the target frequency range. Rectangular part is made even smaller in order to shift its resonance further from the working frequencies range.

Frequencies above 0.5 THz means that the dimensions of metalized areas of the device need to be reduced to tens of micrometers. Also conventional bonding wires

Therefore, phenomenological sensitivity evaluation model can be “corrected”, by including the frequency dependent ratio of the electric field amplitude squared at different frequencies (Fig. 3). As one can see, this curve better matches experimental results than in case of “uncorrected” model. Antenna coupling related effects are responsible for the deviations from the monotonical frequency dependence of the sensitivity within 1–2 THz range. It is also important to note that when evaluation of the data

become too “massive” for the direct bonding since they act as antennas with properties dependent of angle and radii. It is difficult to expect the stable sensor properties due to fixed conductor acting as an additional antenna. All these considerations led to new design. The apex of the BT diode was formed of 5  $\mu\text{m}$  width.  $100 \times 100 \mu\text{m}^2$  bonding pads were shifted 200  $\mu\text{m}$  away from the BT diode and connected via 10  $\mu\text{m}$  contact stripes (Fig. 4).

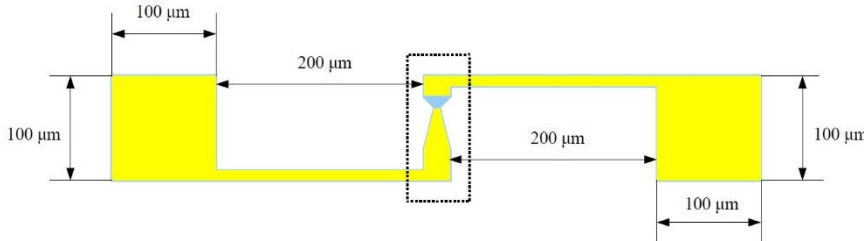


Fig. 4 Design of modified bow tie sensor.

For terahertz imaging systems not only the individual detector characteristics, but also the ability to manufacture the

sensors arrays are important. Investigation of the BT diode operation in dense array is needed. The simulation results are shown in Fig 5. We found that the coupled electric field spectrum was essentially the same for all distances calculated, despite only 20  $\mu\text{m}$  remaining between the nearest metalized parts of array, a case  $L_z=120 \mu\text{m}$ . This is essential result for the array production; the sensors can be packed sufficiently close to each other at least in 1D vector. In a case of higher frequencies (around 0.7 THz), the differences are much smaller and do not exceed 20 % of the average value [K 33].

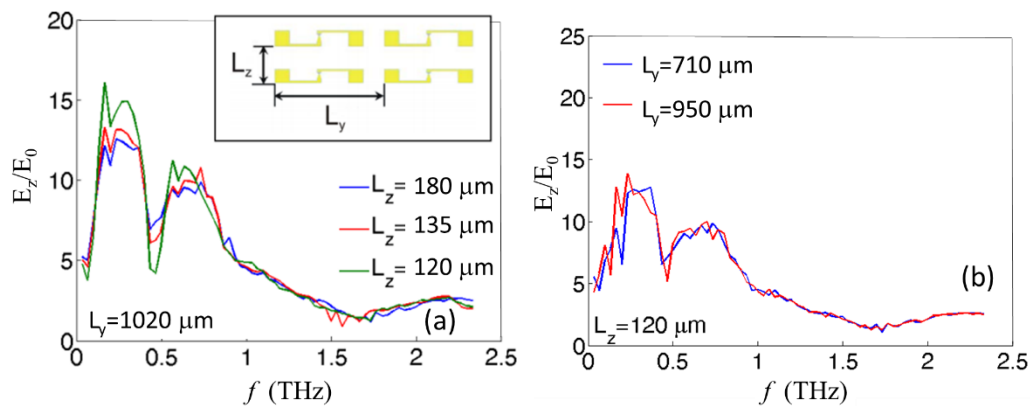


Fig. 5. Dependence of electric field amplitude in the vicinity of BT diode apex on frequency for  $L_y=1020 \mu\text{m}$  and several periods of  $L_z$ . Inset: illustration of used notations  $L_z$  and  $L_y$  (a). Dependence of electric field amplitude when  $L_z=120 \mu\text{m}$  is fixed and the  $L_y$  was varied. [K 33]

The presence of the resonance at 0.5 THz frequency origin is related to larger elements of quite complex detector structure, contact pads and bond wires. To test further reduction possibilities of the area devoted to each detector, the  $L_z=120 \mu\text{m}$  was fixed and

the period in  $y$  axis direction was varied. The calculation data is shown in Fig. 5 b. Reduction of the area by approximately of  $1/3$  distorts the electric field amplitude spectrum at 0.2 THz, but it stays nearly constant in the region above 0.5 THz.

### **2.3 Chapter summary**

To summarize, Finite-difference time-domain simulation results of electric field amplitude dependence on frequency in bow-tie shaped InGaAs detectors active area were presented. It was shown that two metalized parts of the bow-tie type detector act as the separate antennas. Simulation results of the crosstalk effects between detectors in arrays allowed to choose an appropriate distances to adjacent sensors. These results allow to form the *first statement to defend*.

The electric field amplitude at the apex of antenna has the greatest impact for the experimentally observed bow-tie shaped InGaAs detector sensitivity reduction above 1 THz; moreover, the sensor metallized areas act as two separate antennas with their own resonances.



### 3 PROCESSING OF SAMPLES AND THEIR CHARACTERIZATION

#### 3.1 The structure of bow-tie sensors

InGaAs samples were grown using molecular beam epitaxy and processed as described in [IP 6]. Parameters of investigated samples are summarized in Table 1.

Table 1. Description of the InGaAs samples.

Sample	Thickness of InGaAs, nm	x (In)	Type and concentration, cm <sup>-3</sup>	InAs monolayer	Fabricated at
I197	540	0.47	position dependent	No	FTMC
I204	500	0.532	position dependent	Yes	FTMC
I13169	520	0.53	$n = 2.4 \times 10^{14}$	Yes	Fraunhofer

InGaAs 500 – 540 nm thick and a monolayer of InAs were grown on 500  $\mu\text{m}$  thick InP (001) substrate. Mesas were formed using wet chemical etching. For the metallization, a Ti layer with thickness of 20 nm and an Au layer with thickness of approximately 180 nm were deposited as a two-layer structure. The gap between the contacts above and below the active area was set to 10  $\mu\text{m}$  for all samples with exception of I204 during photolithography mask production, but was slightly smaller in finished devices due to processing peculiarities.

Typical bow tie sensor structure is shown in Fig. 6. It consists of the contact pads, which are normally at a distance of 200  $\mu\text{m}$  from detector`s active part, an antenna, which designs and modifications are different, and the InGaAs active region. The antenna shape is not symmetrical, it consists of narrowing metallized area. Its aim is to concentrate the THz radiation in the active area, consisting of InGaAs and InP heterostructure. Samples were mounted on specially designed chip holders for further electrical investigations. Detailed image of bonded samples is presented in the bottom of Figure 6.

#### 3.2 Electrical characterization of BT sensors

Detailed electric characterization of high-performance InGaAs-based terahertz radiation detectors and corresponding simulation results are presented. The local surface potential and tunneling current were scanned on the surface of detectors by Kelvin probe force microscope (KPFM) [19] and scanning tunneling microscope (STM) and a position of the Fermi level was obtained from these experiments. Current-voltage curves were

measured and modelled using Synopsys Sentaurus TCAD [20] package to get a better insight of processes happening within the detector. In addition, finite-difference time-domain simulations were performed to reveal the peculiarities of electric field concentration by the metal contacts of the detectors.

### 3.2.1 BT sensor energy band diagram

A scheme of the expected band variation across the tested structures is graphically presented in Fig. 7.

Several main features of energy levels, sketched in Fig. 7, could be mentioned. First, work function value of Ti is smaller than electron affinity of InGaAs, therefore, potential well for electrons is formed near the interface between these two materials and ohmic contact should be formed in case of *n*-type InGaAs. Previous study of ohmic Ti/Pt/Au contact stability on InGaAs was confirmed in [21].

Therefore, due to the complex shape of this multilayer device, there is no easy analytical solution for the exact potential distribution. Sentaurus TCAD simulations were performed to compute numerically possible distributions of electrostatic potential for several scenarios involving different overlaps of metal layers and surface charges.

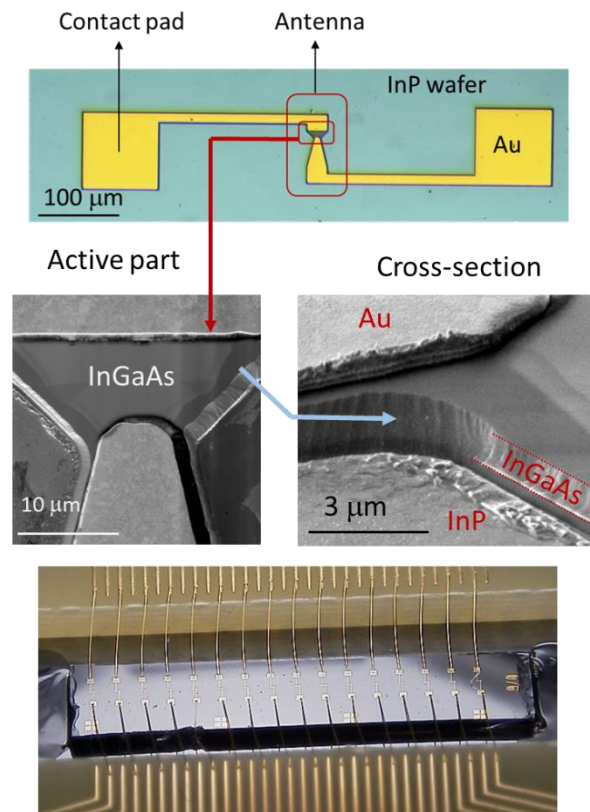


Fig. 6. The layout of bow tie sensor (Top). SEM image of the active part of the sensor (middle). Image of bonded bow tie matrix on the chip holder (bottom).

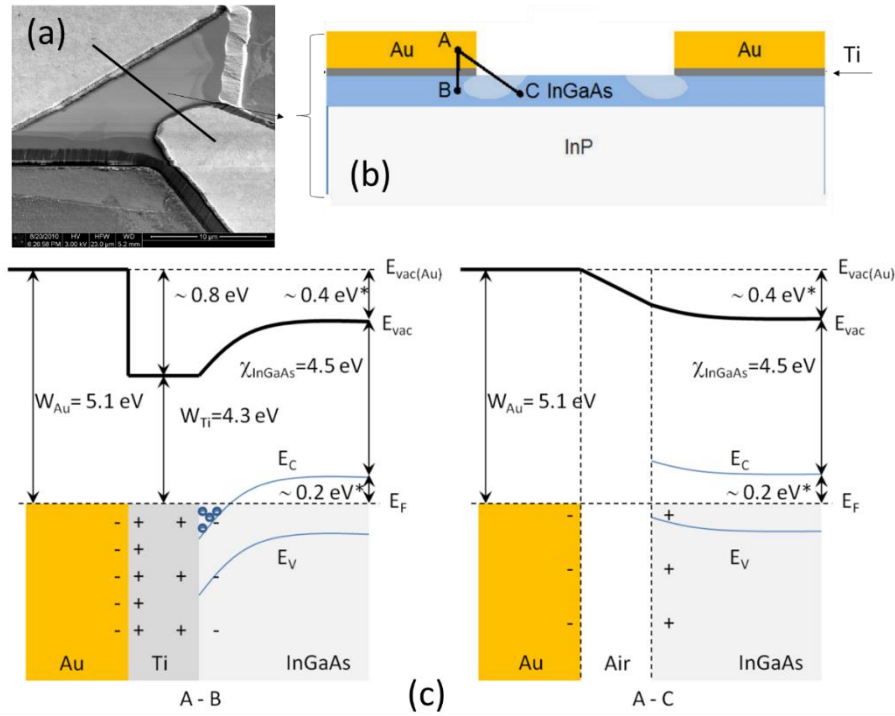


Fig. 7. SEM image of the active part of the BT sensor (a). Line indicates the approximate position for the cross-section (not to scale) sketch (b). Letters "A", "B", "C" mark the ends of cross-sections for which electrostatic analysis will be performed. Lighter blue areas mark approximate positions of InGaAs areas in which Au contact edge might influence carrier concentration due to electrostatic effects. Sketch of the expected vacuum energy level (thick line) dependence on coordinate without applied external voltage (c). Left: along A – B line. Right: along A – C line. (\*) marks estimated values for the case of low doping and assuming no surface charge or Fermi level pinning. [PS 1]

### 3.2.2 Kelvin probe measurements

Dependence of the difference between the surface work function and the left contact work function on the coordinate along the line indicated in Fig. 7 was measured using Veeco Dimension 3100/Nanoscope IVa Atomic Force Microscope. Obtained results for I13169 sample with applied 0.3 V external voltage and both samples without an external voltage are presented in Fig. 8. As one can see, work function difference gradually raises within first 1  $\mu\text{m}$  from the metal edge reaching approximately 0.4 eV and  $> 0.2$  eV difference in comparison with the gold surface in case of samples I204 and I13169, correspondingly. At the same time, much smaller potential differences are observed for sample I197. A sketch of expected results based on Fig. 7 is also depicted in this figure. One can easily observe the difference of at least several hundred meV in the center between the contacts. Such a large difference could either suggest that Fermi level is

located several hundred meV lower than initially estimated, or that observed results are influenced by additional factors such as surface states and surface charges.

### 3.2.3 STM measurements

Surface Fermi level position and surface density of states (SDOS) were also evaluated by means of scanning tunneling spectroscopy (STS) technique. Results of these measurements are presented in Fig. 9. As one can see, normalized derivative of the tunneling current starts increasing at approx. 0.4 V and -0.3 V. Difference between these voltages is consistent with the bandgap of InGaAs sample and voltages corresponding to higher SDOS regions could indicate, that Fermi level is located only slightly below the middle of the bandgap. The difference of 0.4 eV between Fermi level and the bottom of the conduction band with 4.5 eV electron affinity would lead to approximately 4.9 eV work function, so the missing several hundred meV have to be found for sample I13169 to explain the work function dependence on coordinate in Fig. 7.

Similar difference of several hundred meV between STS and KPFM results was already noticed previously with InGaAs and attributed to a fixed charge of  $7.3 - 12 \times 10^{12} \text{ cm}^{-2}$ , shifting of Fermi level in case of KPFM and much lower sensitivity of STS to surface charges [11]. Since comparable differences between STS and KPFM results are obtained in case of our samples, we will employ similar values of

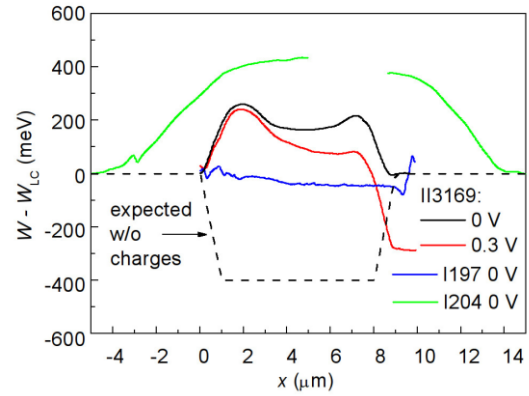


Fig. 8. Work function dependence on distance between the metal contacts of bow-tie detectors. Solid lines – KPFM measurement results, dashed line – sketch of the expected (without the influence of surface charges). [PS 1]

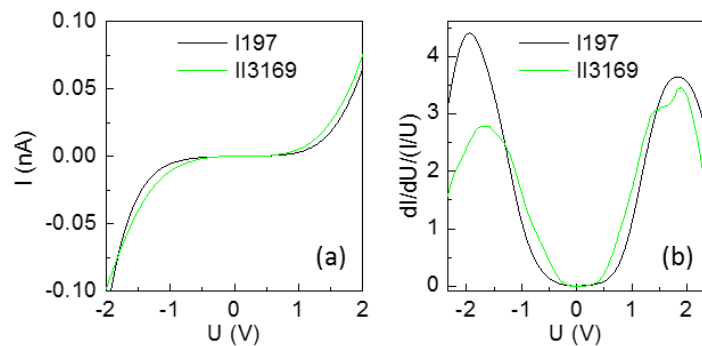


Fig. 9. Dependence of the tunneling current (left) and its derivative (right) on the sample bias. [PS 1]

surface charge in our simulations presented later.

### 3.2.4 Bow tie IV characteristics

IV characteristics of the investigated samples are presented in Fig. 10. Two major features are apparent: difference of nearly two orders of magnitude between differential resistances at 0 V point and IV curve bending for the sample with higher resistance once voltage approaches the value of 1 V. This let us to evaluate  $n = 7 \times 10^{13} \text{ cm}^{-3}$  averaged concentration estimation for 0.5  $\mu\text{m}$  InGaAs layer thickness. The estimated potential

difference required for a full depletion between the bottom and the top of the InGaAs layer is equal to 13 mV. A corresponding value of electron potential energy difference (13 meV) is more than one order of magnitude smaller that work function differences between experimentally measured values and expected ones (Fig. 8), so one can expect that surface might play a crucial role defining the electrical properties of our sensors.

IV simulations using Sentaurus TCAD [20] were performed in order to reveal possible phenomena leading to observed experimentally IV curves. Since low apparent conductivity of the samples correlate with FET-like current limitation in the IV curves, two main factors possibly appearing as a result of device fabrication were considered.

The first one is the Au layers overlap over Ti sublayers possibly taking place during gold deposition process. As a result of larger workfunction of Au (5 eV) than the one of Ti (4.3 eV) the Schottky barriers are formed around Ti contact sublayers thus impeding the movement of electrons from one Ti contact sublayer to another upon application of voltage. The second considered device feature which may affect the character of IV curves is the surface charge appearing at the top surface of InGaAs channel between the contacts.

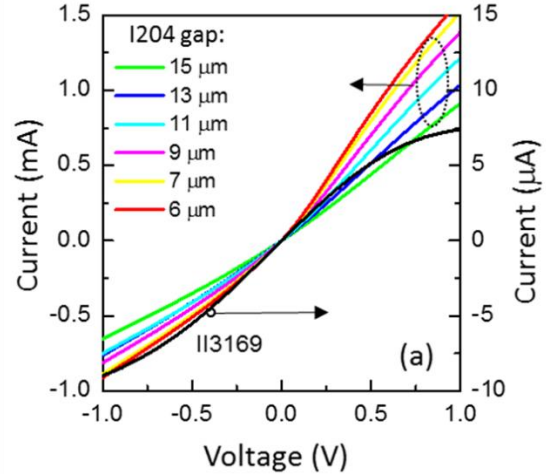


Fig. 10. IV curves of the bow tie sensors made of II3169 and I204 wafers. The gap shows the length of active part in bow tie sensor made of I204 wafer. [PS 1]

The negative surface charge (expected from Kelvin probe measurements) creates the negative electrostatic potential forcing electrons to move away from InGaAs surface and reducing the thickness of the conductive part of the channel.

First electrostatic (with zero applied external voltage) simulations were attempted with variable metal overlap and with variable semiconductor doping as another parameter. Schottky barrier and depleted region are formed below gold contact due to relatively high work function of gold. This depleted region covers an entire channel once an overlap is increased to 1  $\mu\text{m}$ . At higher doping levels, as expected, size of this depleted region is reduced due to higher density of charges and therefore – screening of the electrostatic fields by thinner charged layers [PS 1]. However, such simplified analysis is obstructed by the fact that InGaAs layer thickness is of the same order as metal thickness and radius of the curvature near the edge, so short channel type transistor operation and full numerical simulation has to be considered.

Simulation results for several metal overlaps and doping concentrations confirm previously expressed reservations about Shottky-type gate, obtained using just metal overlap. An additional problem emerge once sample bias is increased, thickness of depleted region grows near one of the metal contacts, channel width is reduced there and the largest potential drop is obtained near this contact. This contradicts somewhat with our previously presented in Fig. 8 results, where rather gradual drop of the additional potential difference is observed [PS 1].

These both factors lead to a further model refinement – possible influence of surface charges of the open InGaAs surface was considered in order to numerically simulate larger (along  $x$  axis) partially depleted InGaAs area. Several simulation results looking closest to FET type of IV are presented in Fig. 11. As one can clearly see, introduction of relevant surface charges leads to the required IV curve shape bend. However, the parametrical dependence of IV curves shape has significantly different character which is defined both by the value of doping and the width of the InGaAs channel. For the fixed width of the channel and high doping levels (Fig. 11 c) the larger surface charge decrease the value of current. Not so in the case of lower doping for the same width of the channel (Fig. 11 a). The values of current are by two orders lower in the presence of the surface charge and the current itself parametrically increase with the increased surface charge. Such a

different behavior of IV curves takes place when the depletion region width becomes equal or larger than the width of InGaAs channel. In such a situation the major carriers dramatically lose their role in the total current and the parametrical increase of current takes place due to the increasing values of minor carriers concentration. However for the same doping level situation changes if the InGaAs channel width is enlarged to be wider than the depletion region. As shown in Fig. 11 b the parametric IV dependencies for the device with the thicker InGaAs channel are the same for both doping levels.

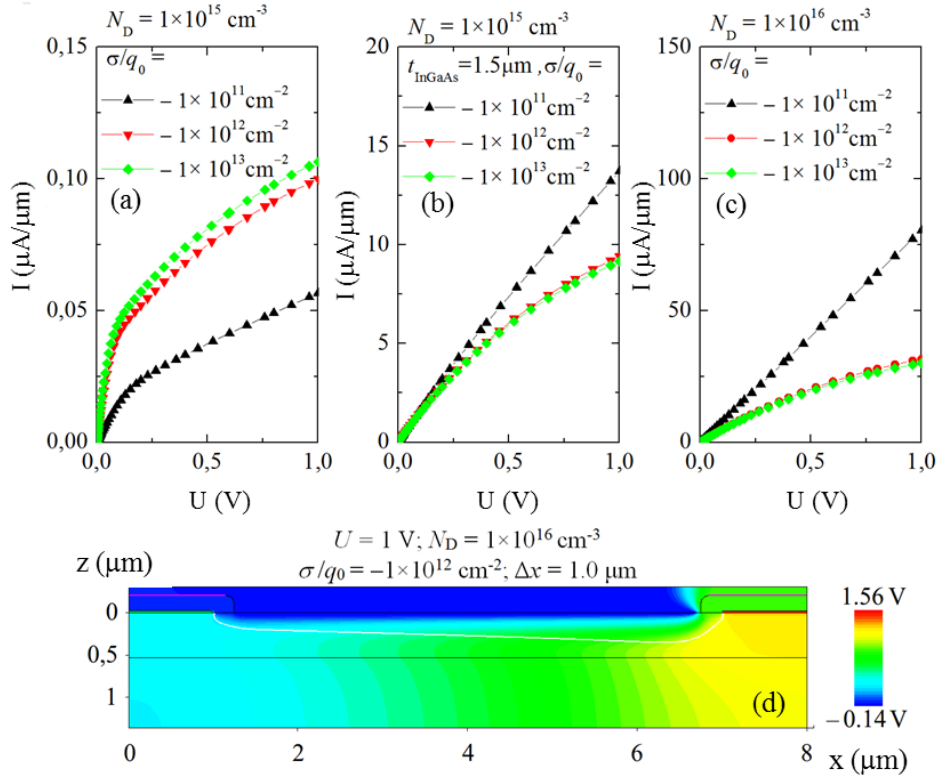


Fig. 11. Simulated IV curves for several doping levels and surface charge densities (a-c). Distribution of electrostatic potential within the device in case of 1 V sample bias,  $0.25 \mu\text{m}$  overlap,  $N_D = 1 \cdot 10^{16} \text{ cm}^{-3}$  doping and  $\sigma = 1 \cdot 10^{12} q_0 \cdot \text{cm}^{-2}$  surface charge density. [PS 1]

In addition we paid the special interest to the mobility of electrons in our simulations. The values of electric field presented in the studied devices are large enough to affect the charge mobility. Therefore, we separately studied the high-field depending mobility effect on the shape of IV curves. Simulation results confirmed that negative differential resistance at high fields above  $3 \text{ kV/cm}$  alone isn't sufficient to produce the experimentally observed VI shape of sample with higher resistance [PS 1].



### 3.2.5 Bow tie sensor detection model supplement by dual FET self-mixing effect

After the model for DC current-voltage characteristics is established and suitable ranges of parameters are defined, one can turn to high frequency AC models. Finite difference time-domain simulations were performed to reveal the expected distributions of electric field amplitude near the metal tips. Obtained distribution of electric field amplitude within InGaAs detector is presented in Fig. 12. As one can clearly see, electric field is mainly concentrated near the edge of the sharper metal contact. This AC field acts as a high frequency voltage source between the gate and source of the equivalent FET. Vertical electric field component  $E_y$  is responsible for modulation of channel conductivity. AC current induced by  $E_x$  in-plane field component is therefore partially rectified to produce an observable DC component. The second transistor on the other side of device is also acting as a FET detector, however, its influence is reduced due to much lower electric field amplitudes. Such detection mechanism has similarities with recently demonstrated one for junctionless FETs [22]. However, in our case the edge of the metal contact acts as a compact gate, while an equivalent of DC gate-source voltage would be "provided" by metal work function differences and open surface charges.

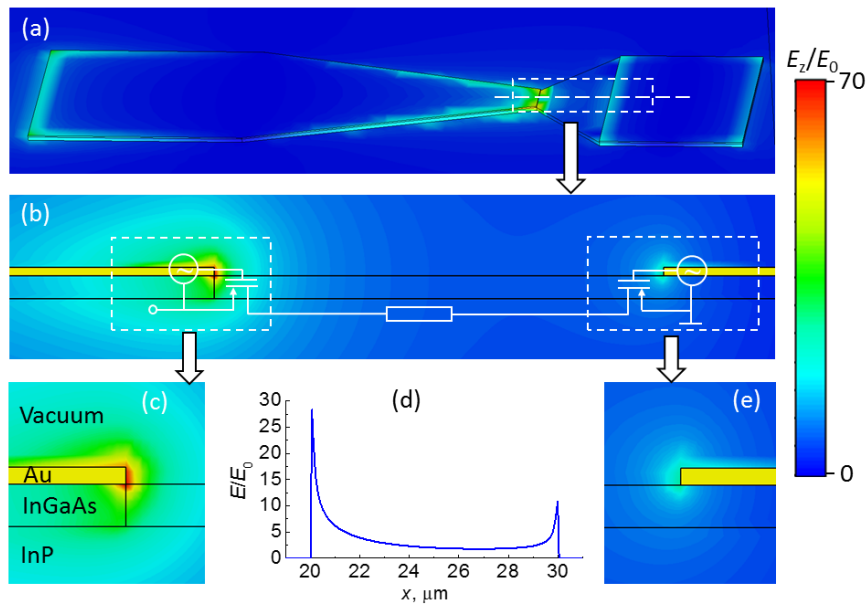


Fig. 12. Distributions of electric field amplitude within the detector at 0.57 THz (a); enlarged part of the top panel and a sketch of equivalent circuit (b); distribution of electric field amplitude near metal contact edges (c, e) and the dependence of amplitude on the coordinate along the symmetry axis of the active part (d). Dashed lines indicate an approximate location of areas to be enlarged in the following panels of the figure. [PS 1]



### 3.2.6 Influence of DC current on detector's sensitivity and noise

Several important detector properties can be expected based on simulation results presented in Sections 3.2.4 and 3.2.5. First, if channels of both "FET-like" device parts are indeed partially conductive without applied external voltage (as expected from IV's of Fig. 10) and if potential reduction of the corresponding metal electrode can "squeeze" selectively one of them, one would expect a possibility of tuning of resistive self-mixing performance of both "FET-like" parts by changing applied DC voltage. Also, both "FET-like" parts are connected in series and would produce rectified voltage of opposite signs, so the voltage of the rectified signal should change sign when switching from pitch-off of one "FET" to another. For DC voltages between these two regimes, detector signal should change gradually and reach zero for equal contributions of both parts of the device.

To experimentally verify these assumptions detector was illuminated by focused 0.58 THz radiation. AC signal from the detector was collected using Signal Recovery 7265 lock-in amplifier operating at 10 s integration time. Both in-phase and out-of-phase signals were recorded together with noise data. Obtained results are presented in Fig. 13. As expected, sign of the in-plane voltage signal changes at approximately  $-4 \mu\text{A}$  when increased resistive self-mixing performance of the "wider-FET"

compensates the influence of better electric field concentration (illustrated in Fig. 12) within the narrower one. Noise increase at higher voltage levels could also potentially serve as an additional evidence of channel resistance increase.

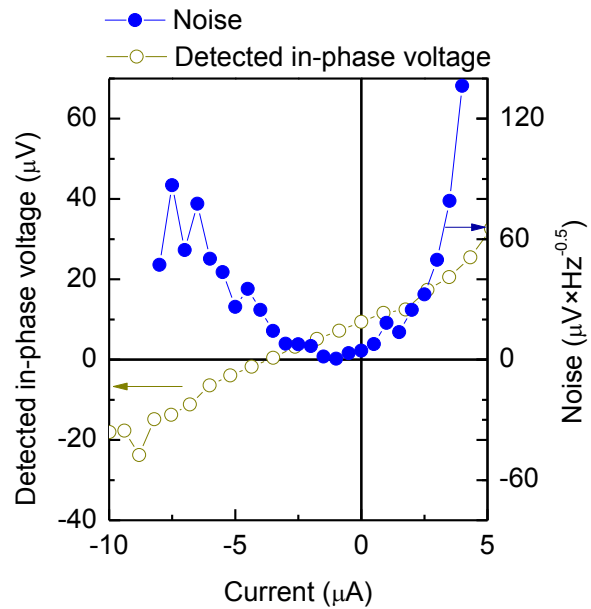


Fig. 13. Dependence of the detected signal and noise on applied DC bias voltage at 0.58 THz. [PS 1]

### 3.3 Chapter summary

Detailed electric characterization of high-performance InGaAs-based terahertz radiation detectors and corresponding simulation results were presented. The local surface potential and tunneling current were scanned on the surface of detectors by Kelvin probe force microscope (KPFM) and scanning tunneling microscope (STM) and a position of the Fermi level was obtained from these experiments. Current-voltage curves were measured and modeled using Synopsys Sentaurus TCAD package to get a better insight of processes happening within the detector. In addition, finite-difference time-domain simulations were performed to reveal the peculiarities of electric field concentration by the metal contacts of the detectors. These results allow to form the *second statement to defend*.

The shape of current-voltage characteristics and changes of the detected signal due to bias current of bow-tie InGaAs sensors, made of InGaAs layer of more than 50 k $\Omega$ /sq sheet resistance are caused by field effect due to surface charges.

## 4 TERAHERTZ DIRECT AND HETERODYNE IMAGING WITH InGaAs BOW-TIE SENSORS

Room-temperature detection and imaging in transmission and reflection geometries at 0.59 THz with planar asymmetrically-shaped InGaAs diodes are demonstrated in direct and heterodyne mode. Also imaging using 32 sensors array with integrated low noise amplifier will be considered.

### 4.1 Set up for direct and heterodyne detection

The set-up for imaging experiments at 0.59 THz is shown in Fig. 14 a. Two electronic sources of THz radiation for heterodyne imaging are required. The first one (LO source) was based on a frequency-stabilized Gunn oscillator working at 591.400 GHz. The other (RF source) was based on a frequency-synthesizer source whose signal was multiplied by a factor of 36 and operated at a frequency which was larger by intermediate frequency  $f_{IF}$  than the LO frequency. In most measurements,  $f_{IF}$  amounted to 43.964 kHz. Beam splitters (D1 and D2) guided 10 % of the incident power from each source to a reference detector. The remainder of the radiation of the RF source was focused onto the object under test and then collected by mirrors and focused onto a silicon lens on top of a BT diode for detection. In heterodyne measurements, the radiation from the LO source was overlaid onto the RF beam via the 60:40 beam combiner D3. The object was mounted on a computer-controlled x-y translation stage for raster-scan imaging. In direct-detection mode, only the RF source was used. The beam was mechanically chopped at a frequency of 2 kHz for lock-in detection [IP 6].

### 4.2 Bow-tie sensitivity estimation

Firstly, the sensitivity of the BT detector was determined. The optical sensitivity was estimated using the methodology described in [23]. The optical sensitivity was found to be 6 V/W. For determination of the NEP, RF beam was gradually attenuated and then voltage signal of the detector was measured. The data are shown in Fig. 14 b (blue stars). The noise bandwidth was 2 Hz. The minimal detectable power was 2.5 nW which results in a NEP value of 4 nW/ $\sqrt{\text{Hz}}$ . Corresponding data for heterodyne detection is also shown

in Fig. 14 b. It was estimated that about  $11 \mu\text{W}$  was delivered to the diode. Upon attenuation of the RF beam, and for a noise bandwidth of 2 Hz, the lowest detectable power was  $230 \text{ fW/Hz}$  (green circles of Fig. 14 b) [IP 6].

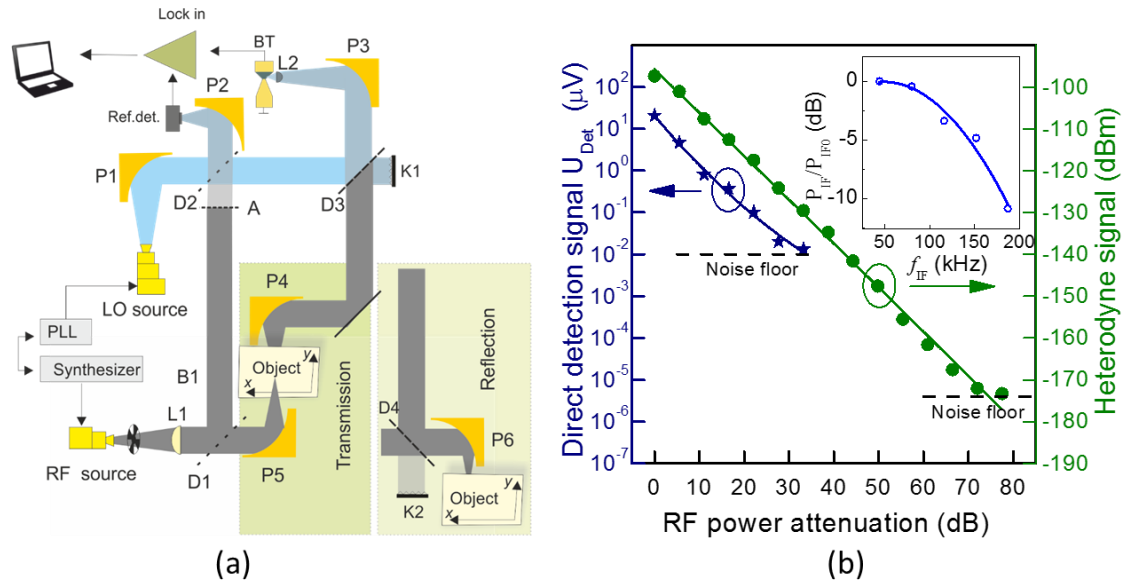


Fig. 14. Set-up for terahertz imaging in transmission and reflection geometries using direct and heterodyne modes (a). Letters D denote beam splitters, BT – bow-tie diode, A – absorbers, L – lenses, P – parabolic mirrors, A – attenuator, PLL – phase lock loop. Attenuation in direct detection (stars) and heterodyning mode (circles) (b). Horizontal dash line depicts noise floors. Upper inset: IF signal (circles) for various intermediate frequencies between 43 kHz and 180 kHz. [IP 6]

The difference in minimal detectable power between heterodyne and direct mode amounts to about 43 dB. The upper inset of Fig. 14 b depicts the dependence of the heterodyne signal on  $f_{\text{IF}}$  for a fixed LO power of  $11 \mu\text{W}$  on the sensor. The 3-dB point is found to be at 100 kHz; while the response time of the diode is 7 ns [16]. The signal rolls off towards higher  $f_{\text{IF}}$  due lock in amplifier frequency range [IP 6].

### 4.3 THz images in transmission and reflection modes

Images obtained with the BT diode as a detector at 0.59 THz are shown in Fig. 15. THz transmission images of a leaf placed in an envelope is shown in the left side of Fig. 15. For this weakly absorbing object, the advantage of heterodyne detection (Fig. 15 c, d) over direct power detection (Fig. 15 b) lies mainly in the ability to obtain phase images. The contrast enhancement in the power image is not readily discernible. This is different for the reflection images of a coin in a paper envelope shown in right site of the Fig. 15. The

RF beam power was attenuated which resulted in a grainy image close to the noise floor in direct-detection mode. The image obtained in heterodyne mode (Fig. 15 right side b) is free from the grainy structure because of the higher – on the order of 20 dB – dynamic range. In the phase image (Fig. 15 right side d), the coin’s relief is well resolved, and looks impressive. Perhaps it was the main point why editors of the journal of Applied Physics Letters selected as a cover magazine image [IP 6]. However, the image is diffuse at the rim where the height becomes comparable with the wavelength of the illumination.

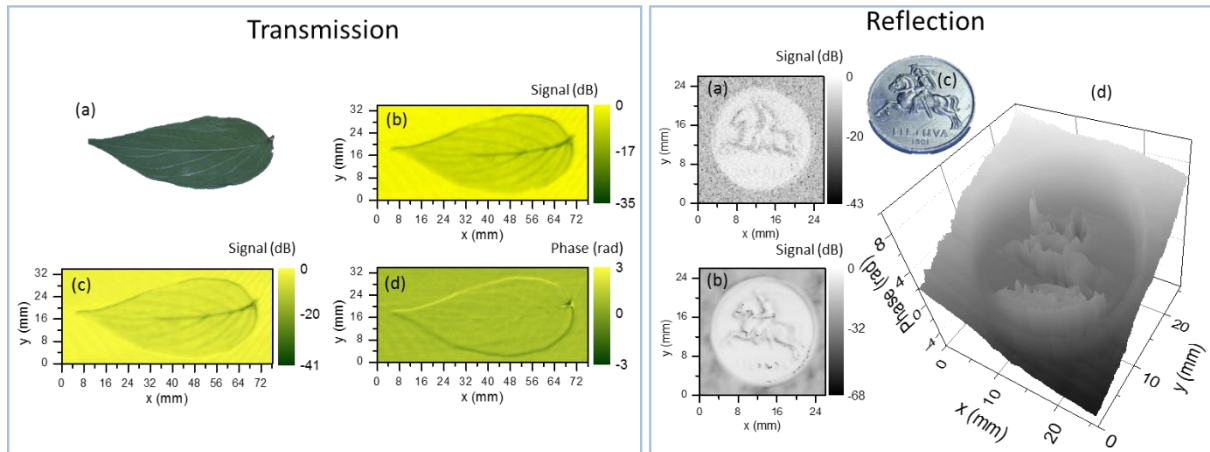


Fig. 15. Left – 0.59 THz transmission images of a leaf placed in a paper envelope: photograph of the leaf (a); direct power detection scheme, power image, heterodyne mode (b); and (c) phase image, heterodyne mode. Right – 0.59 THz reflection images of a Lithuanian 1-cent coin placed in the paper envelope: (a) direct mode; (b) power image, heterodyne mode; (c) photograph of the coin; (d) phase image, heterodyne mode. [IP 6]

#### 4.4 Imaging with array of 32 BT sensors

In order to reduce THz imaging time, the need to combine BT detectors into arrays, emerged. In case of one sensor, the signal was registered by lock in amplifier. Such solution is not suitable for sensor arrays, since each channel requires a separate lock in amplifier. Therefore, 32-channel low noise amplifiers chain with band pass filters for the detectors parallel signal recording were constructed and combined with BT array chip. The principal scheme for one channel read out electronics and whole box of chip and electronics are summarized in Fig. 16. The photo of 32 sensors matrix with integrated low noise amplifiers is presented in the bottom of Fig. 16.

THz imaging experiments with the sensors array was performed. The imaging set up is very similar to direct imaging case set up presented in Fig. 14 a. Beam energy flux density distribution is measured with all sensors at the same time. Maximum response of each sensor in the matrix at 300 GHz (blue line) and at 600 GHz (red line) is presented in Fig. 17 a. As we can see, the detector response depends on the position in the matrix. This effect could be caused by insufficient mask alignment due to relatively long length of the matrix. In this case, the uneven etching process can cause geometrical changes in the active part of BT sensor.

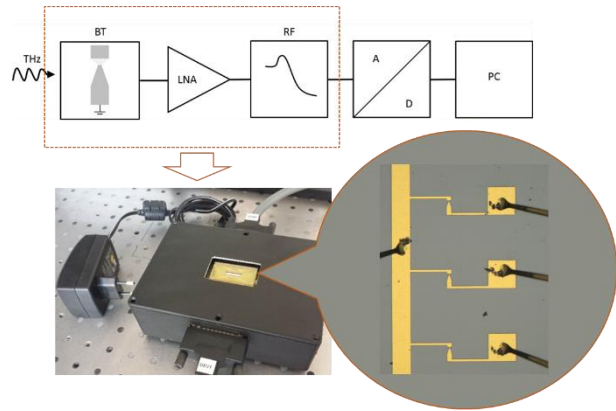


Fig. 16. A principal scheme of detected signal registration (Top), BT – THz sensor, LNA – low noise amplifier, FR – filter, AD – analog-code inverter, PC – computer. The photo of 32 sensors matrix with integrated low noise amplifiers (bottom).

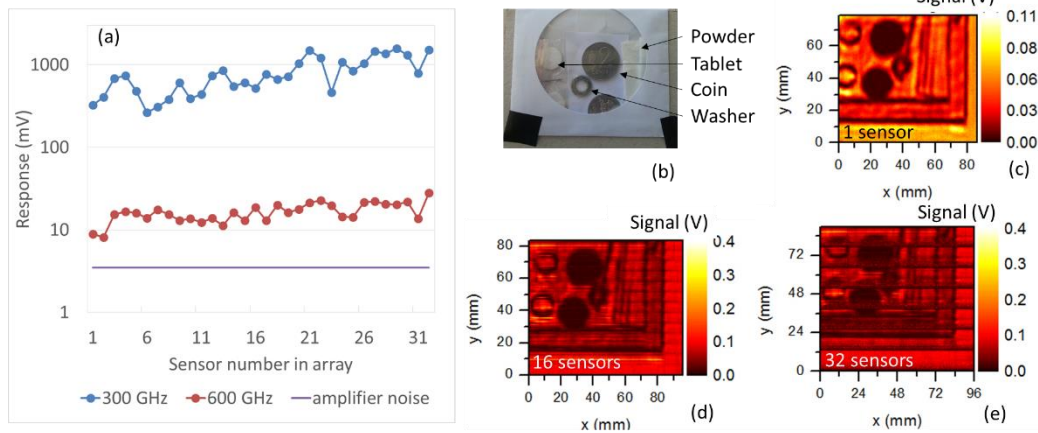


Fig. 17. Maximum response of each sensor in the matrix at 300 GHz (blue line) and at 600 GHz (red line) (a). Photo of the packed sample (b) 300 GHz Transmission image of the sample at 0.3 THz obtained with one sensor (c), half of array (d) and with all sensors in array (e).

The 0.3 THz images of tablets, coins, washers and powder (Fig. 17 b) recorded using BT sensors array are presented in Fig. 17 c-e. For the image quality comparison, the same object THz image was obtained using one sensor of the matrix, half of the matrix and with all sensors in a matrix. The imaging time of the sample using all sensors in the matrix can be reduced 32 times comparing with the case of one sensor. As we can see from Fig. 17, THz

image contours are similar in all cases and objects position in the envelope could be easily distinguished. The noise in the image caused due to the different sensors sensitivity not in all practical application cases, is a decisive factor, comparing with the advantage of increased imaging speed.

#### **4.5 Chapter summary**

Bow-tie shaped InGaAs sensors applications in direct and heterodyne imaging modes in transmission and reflection geometries at 0.59 THz were presented. Moreover, the detectors sensitivity and noise equivalent power were estimated. Also imaging system dynamic range improvement in heterodyne detection mode was evaluated. Finally, the performance of developed bow-tie sensors arrays with integrated low noise amplifiers were demonstrated.

Described results of InGaAs bow-tie sensors applications in THz imaging systems allow to form the *third and fourth statements to defend*.

System dynamic range improvement above 40 dB in comparison to direct detection scheme can be reached due to reduction of noise influence using optimized bow-tie shaped InGaAs sensors in the heterodyne detection scheme.

InGaAs sensor arrays are suitable for independent readout of detected signals at the frequencies above 0.5 THz due to low influence of adjacent sensors if a period between sensors is at least 135  $\mu\text{m}$ .

## 5 FOCUSING PERFORMANCE OF DIFFRACTIVE ELEMENTS FOR THZ RANGE

In this chapter, the terahertz diffractive elements, their combination with resonance filters and their integration into BT sensors arrays will be discussed.

### 5.1 Diffractive elements

Two designs of zone plates were considered (Fig. 18) – the first contained regular Fresnel’s zones and used for reference purpose, while the second one – the TZP – was designed in such a way that cross-shape apertures of the resonant THz filter were placed in open areas of the regular zone plate providing an additional THz frequencies selection. The first type of the samples were produced using standard photolithography on a 30  $\mu\text{m}$  thick copper coated printed circuit board, after peeling out processed the metallic layer from the substrate. Meanwhile the TZP was fabricated using laser direct writing technique [24] of 30  $\mu\text{m}$ -thick molybdenum film. More details on the TZP fabrication and spectral performance can be found in [IP 4].

Three-dimensional finite-difference time-domain (3D FDTD) modeling was applied to simulate impact of the number of zones – in order to define optimal frequency selectivity. Electric fields ratio

being proportional to the transmission intensity was calculated in the focal point aiming to reveal distribution of the radiation and compare it with experiment. Modeling data is shown in Fig. 19. The results demonstrate nicely focusing of the beam (Fig. 19 a). The bandwidth of electric fields ratio is decreased with the increase of the number of zones whilst peak intensity varies only weakly with increasing zone plate number (Fig. 19 b).

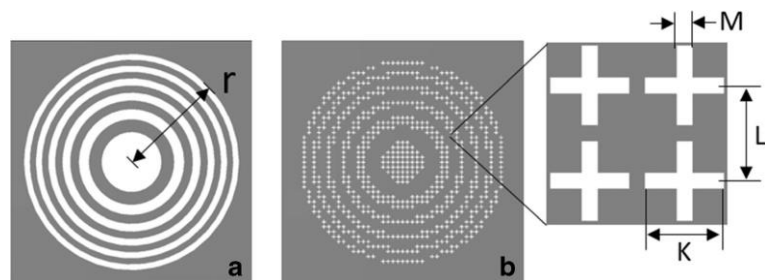


Fig. 18. Layout of the zone plate (a). Combination of the zone plate and laser-ablated resonant filter (b) [IP 2]



Focusing performance of the TZP was measured by imaging a spatial THz laser beam profile in the focal plane with the fast imaging system described [IP 4]. Results are plotted in Fig. 20. It is evident that ripples around the central maximum is smaller for a case of the TZP. The diameter of the

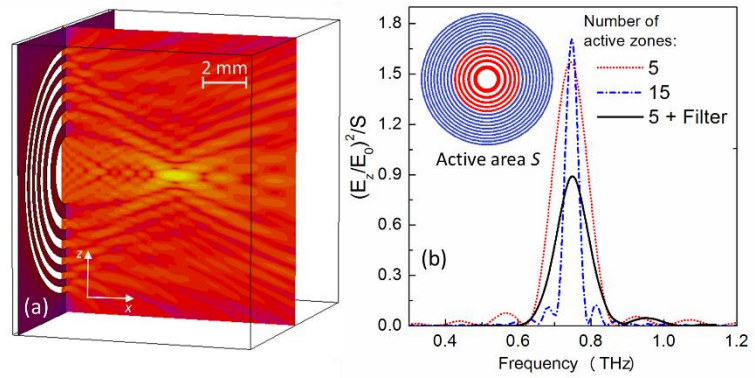


Fig. 19. Electric field distribution in x and z directions behind the zone plate (a). Squared electric field ratio normalized to the area of the zone plate versus THz frequency. [IP 2]

focused beam spot is comparable with that of the conventional zone plate with higher zones number. Due to high numerical aperture (NA=0.62), the spot is focused to diffraction-limited area. Even through the TZP has similar focused beam size as 15 zone plate, the enhancement of the focused beam electric field was found two times smaller, but in a factor of 4 times smaller area of the device. Detector signal enhancement in a factor of 19 comparing with that of the non-focused beam was estimated [IP 2].

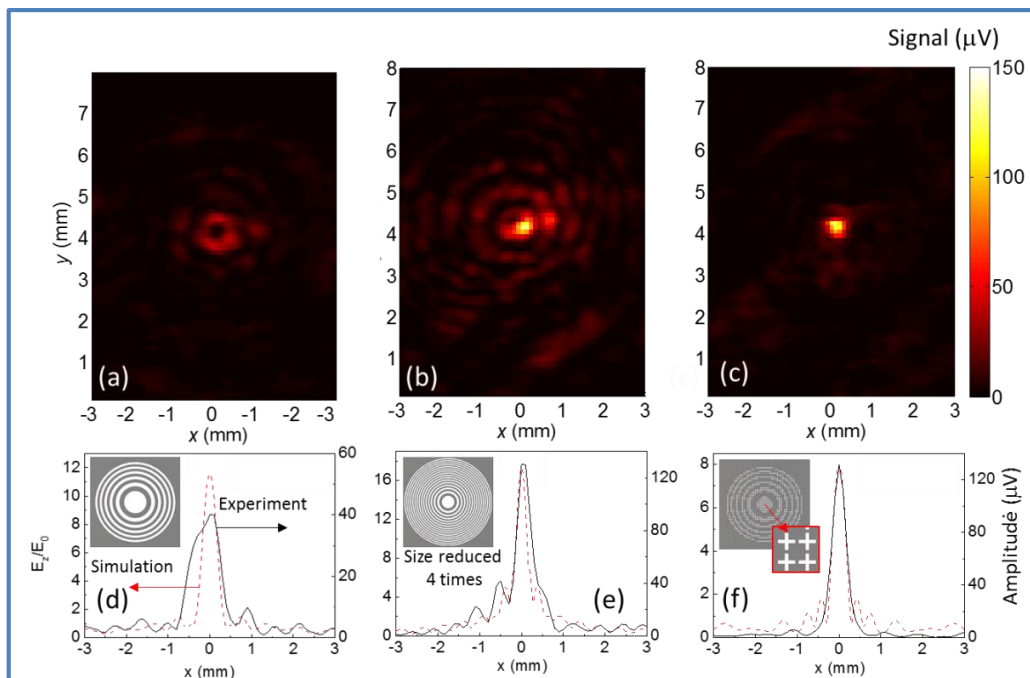


Fig. 20. Images of 0.76 THz laser beam focused with conventional (a, b) zone plates and the TZP (c). Simulated and measured spatial profiles of the THz laser beam at the focal position with conventional 5 (d) and 15 (e) zone plates and with the TZP (f). Insets depict corresponding zone plate design. 15 zones plate size is reduced by 4 times in comparison with others. [IP 2]

## 5.2 High resolution imaging

The performance of the THz imaging system based on the TZP lens versus a commercial off-axis parabolic mirror (PM) was compared by imaging a spatial resolution target at 0.58 THz. The diameter and focal length of the PM were of 2 inches leading to the  $NA = 0.45$ . Imaging results of the resolution target are shown in Fig. 21. It is seen that the system, equipped with diffractive component TZP, provided a much better spatial resolution. Periodic stripes were distinguishable if the period was not smaller than 0.6 mm in the case of TZP lens (indicated by red arrow in Fig. 21); note that the resolution was limited by the wavelength of used THz radiation. And in the case of off-axis PM, the smallest period of stripes was measured of about 0.8 mm. Thus, the imaging system with the TZP lens exhibited improvement in spatial resolution of up to 25 %.

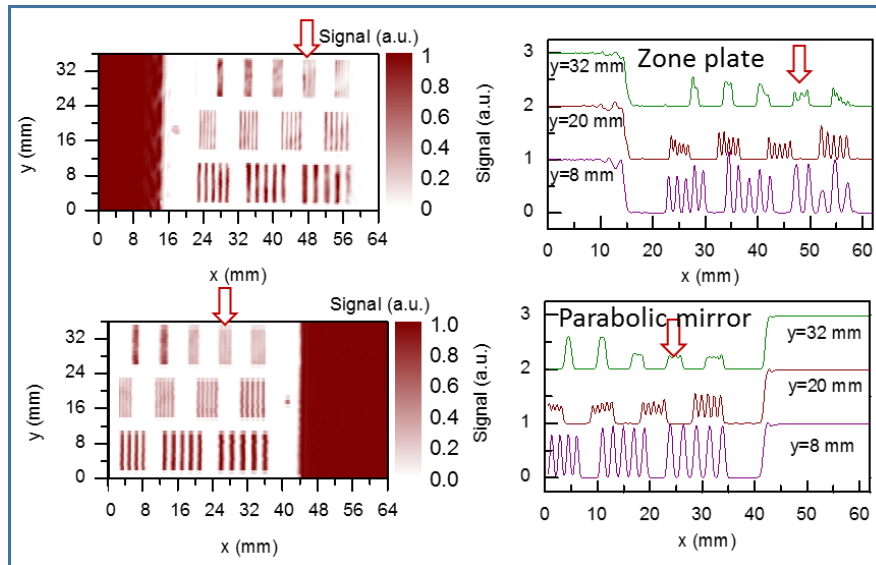


Fig. 21. THz image of the resolution target at 58 GHz frequency obtained by using novel diffractive lenses (a) and commercial PM (c). Black color in the THz images corresponds to the maximum of transmittance. A cross section profile along the  $x$ -axis of the THz image at positions  $y = 8, 20$  and  $32$  mm measured using different lenses: TZP (b) and PM (d). Vertical scales are shifted by 1.

## 5.3 Integrated zone plates on InGaAs bow-tie detectors substrate

A further step in the miniaturisation of the THz imaging system by zone plates integration on the substrate of InGaAs-based bow-tie THz detectors were proposed. The top surface of the InP wafer was used to process the InGaAs detector array using the

previously reported procedure described in chapter 3.1, whereas the bottom metalised surface was structured to provide the focusing elements.

The electric field distribution in the chip and scanning electron microscope images of the zone plate and detector after completing all the processing steps are presented in Fig. 22. Finite-difference time-domain (FDTD) calculations were applied to predict the focusing performance of the integrated zone plate design. (Fig. 22 a). In the SEM image of the zone plate (Fig. 22 b), a 200 nm-thick gold layer appears as areas of lighter grey colour, whereas ablated areas with the open InP surface appear as darker grey shades.

Concentration of the incident radiation was evaluated by the imaging of the spatial beam profile employing the optically pumped THz laser, more detailed experiment set up description is

in [IP 1]. Sensitivity enhancement was experimentally evaluated using a 0.76 THz line of the molecular laser. Variable angle measurements with two detectors were performed to confirm the influence of the zone plate. Results are presented in Fig. 23 (black and red lines). Much lower detection and weak dependence on the angle of incidence were obtained for a detector without the zone plate on another surface of the wafer. For the combined with the zone plate detector, a sharp reduction of sensitivity was obtained when changing the angle of incidence. As the response of the detector is proportional to the power of the incident radiation, squared values of the electric field maxima were used to predict theoretically the angular dependence of the response of the detector (Fig. 23 blue line). Sharp reduction of sensitivity effect is in line with the

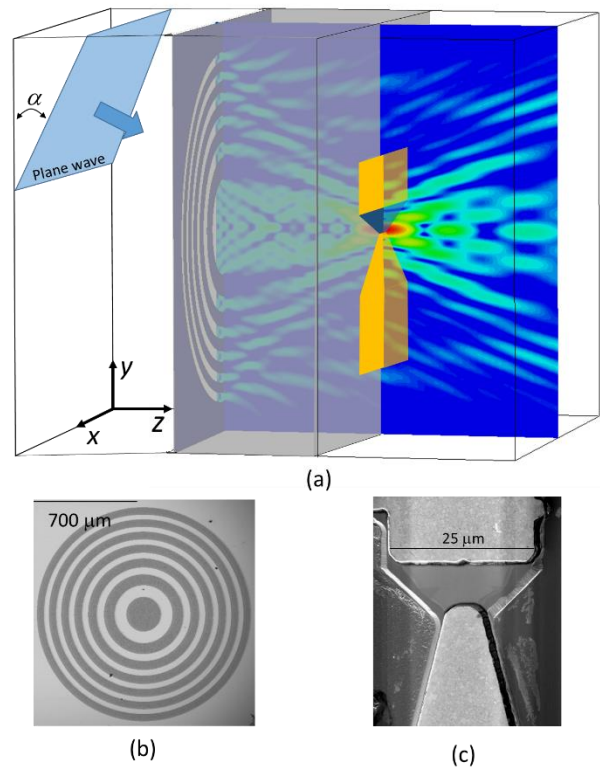


Fig. 22. Schematic image of detector within simulation area and plane wave input position, where  $\alpha$  denotes incident plane wave angle. SEM image of zone plate on bottom InP substrate (b) and bow-tie detector (c). [IP 1]

data, confirming thus that the observed enhancement of the response can indeed be attributed to the influence of the zone plate. Detection enhancement of more than one order of magnitude was obtained due to use of the zone plate, as confirmed by measurements at variable angles of incidence and FDTD simulations of the wave propagation [IP 1].

The above-described experimental and theoretically calculated results confirm that the zonal plate can be successfully integrated into the bow-type InGaAs detector chips. This integration lets to reduce the imaging system optical components quantity. These results were noticed by editors of "Electronics Letters" journal and were published with editorial comments in "Featured article" section of the journal [P 5].

#### 5.4 Chapter summary

Properties of THz zone plates and combined zone plates were simulated numerically and demonstrated experimentally. Their applications in imaging systems can enhance systems resolution up to 25 %. Integration of zone plate with detectors in a single chip allowed to increase the signal by at least an order of magnitude. Presented results allow to form the *fifth statement to defend*.

Modified zone plates for THz range and combined zone plates are suitable for sharp THz beam focusing. Bow-tie shaped InGaAs sensor signal enhancement of more than 20 times and reduction of bulky optical components number in the system are obtained with on-chip integrated zone plates.

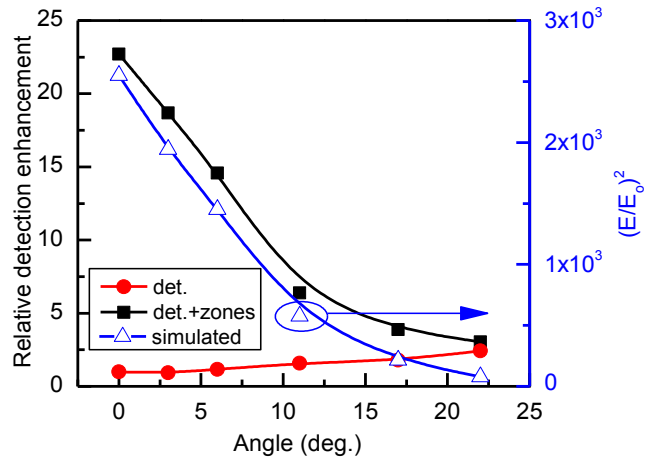


Fig. 23. Detected signal normalised to that of detector without zone plate at angle  $\alpha = 0^\circ$  against incident wave angle. Red line corresponds to detector chip without zone plates and black line to detector with zone plates. Dependence of squared amplitude of electric field on angle, recorded near tip of contact, shown in blue. [IP 1]

## 6 THZ RADIATION APPLICATIONS FOR SOLAR CELLS DIAGNOSTICS

### 6.1 Identification of tab wire soldering defects

Automated soldering of tab wires is a well established technique in modern production lines of silicon solar cell modules. High throughput of these lines also requires comprehensive testing systems for the rapid and accurate inspection of soldering results. However, completely automatic analysis of visible faults is not yet possible, since correct positioning of the tab wire does not guarantee soldering quality [25].

Terahertz time-domain spectroscopy (THz-TDS) [26] may be used to identify the soldered tab wire defects. Such measurement might provide direct information of its height variations. By combining the THz time-domain technique with a data processing tab wire soldering defects in silicon solar cells might be determined.

The terahertz time-domain spectroscopy experiment setup, based on a Teravil-ekspla T-Spec [27] spectrometer, in reflection geometry is presented in Fig. 24. The detailed characterization of the setup is described in [IP 5].

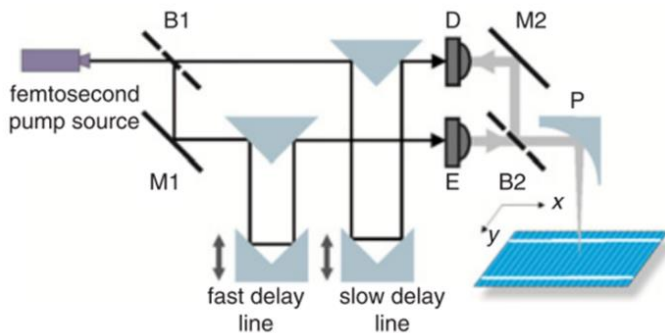


Fig. 24. Measurement setup of T-Spec spectrometer. Thin lines indicate propagation paths of femtosecond laser pulses; thick grey lines – THz pulses. M – mirror, B – beam splitter, P – parabolic mirror, D – detector, E – emitter. [IP 5]

Standard tab wires were soldered on a commercial crystalline silicon solar cell with intentional defects is presented in Fig. 25 a. As one can see from the THz amplitude images in Fig. 25 b, most of the amplitude images of uneven contact sectors are distorted in comparison to neighboring smooth areas. However, such amplitude images are not very reliable for determining the precise places requiring repair work. The terahertz wave phase image, presented in Fig. 25 c, is more informative: all uneven spots appear as the local change in phase, including both loops at sections 2 and 4.

Standard tab wires were soldered on a commercial crystalline silicon solar cell with intentional defects is presented in Fig. 25 a. As one can see from the THz amplitude images in Fig. 25 b, most of the amplitude images of uneven contact sectors are distorted in comparison to neighboring smooth areas. However, such amplitude images are not very reliable for determining the precise places requiring repair work. The terahertz wave phase image, presented in Fig. 25 c, is more informative: all uneven spots appear as the local change in phase, including both loops at sections 2 and 4.



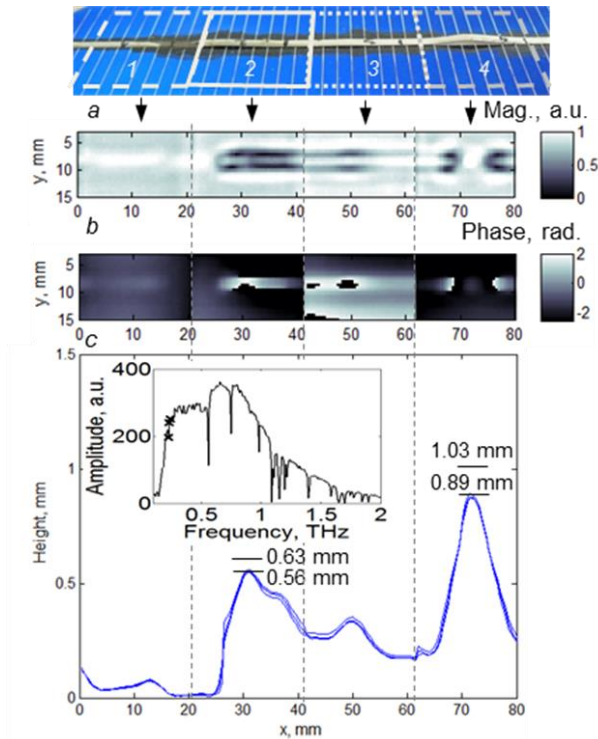


Fig. 25. Images of silicon solar cell sample with tab wires. Photo of sample (a). Lines indicate approximate positions of five THz image segments. THz amplitude image (b) and phase image (c) at 0.243 THz. Tab wire height profile, reconstructed from phase imaging data (d). Short horizontal lines and values indicate real and measured heights of tab wire loops. Spectrum of incident wave is presented in the inset. Markers indicate frequencies used for height estimation [IP 5].

electron microscope images of two etched silicon sample are presented in Fig. 26 a. As one can clearly see from these images, only sub-micrometer scale surface roughness is obtained on the surface of the sample B, therefore emulating the start of the usual structuring process, while surface of the sample A is already nearly fully with “pyramids” of several micrometer size, expected near the end of the structuring process. THz images are presented in Fig. 26 c - e. Localized features are revealed in etched samples at higher frequencies of 1.4 THz and 1.63 THz. Oscillations of reflectivity, obtained when analyzing data for variable frequencies (Fig. 25 b), suggest that interference between top and bottom surfaces of the wafer might be the dominant factor determining the reflectance in THz range.

The difference of heights  $h$  was estimated. Results of such estimation from image data obtained at five indicated frequencies are presented in Fig. 25 d. As one can clearly see, height profiles are consistent with the photograph of the sample. The calculated heights of two loops are 0.56 mm, 0.89 mm for the 0.243 THz frequency. To verify the measurement, heights of two loops in sectors 2 and 4 were measured with a digital caliper and were 0.63 mm and 1.03 mm correspondingly.

## 6.2 Control of silicon etching process

For surface THz imaging experiments several segments of  $\langle 100 \rangle$  oriented crystalline silicon (c-Si) wafers were processed. Scanning

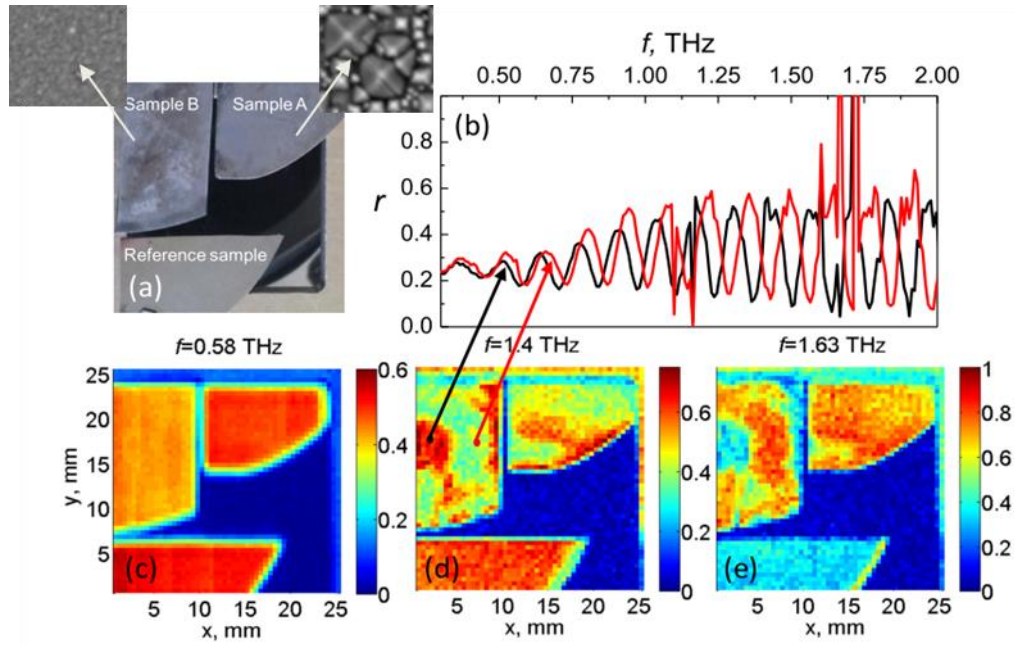


Fig. 26. Photograph of crystalline silicon samples (a). THz reflectance spectra at two points (b) of THz images at several distinct frequencies (c - e). [K 3], [K 18]

### 6.3 Identification of encapsulated solar cell defects module material defects

The characterization of solar cell during fabrication process not always ensures the final solar cell module quality. Therefore, it is worthwhile to evaluate the solar cell and its contacts in the state after module assembly. Glass – glass solar modules are increasingly appearing on the market. They have a longer service life, are more resistant to environmental and mechanical stress than standard modules [28]. Such module was selected for the detailed investigation using THz-TDS setup. Standard industrial silicon solar cell piece partially encapsulated with transparent QSIL216 PDMS-based encapsulate sandwiched between two approximately 1 mm thick glass slides (Fig. 27 a, b). THz images, obtained for the module test structure are presented in Fig. 27 c, d. At 0.46 THz, front glass slide becomes sufficiently transparent to THz radiation, different reflectivities of two areas can be observed and PDMS layer edge can be distinguished. Also different reflectivities of solar cell surface and metal contact can be distinguished. At 0.66 THz, complex refractive index of the front glass slide becomes the dominant factor determining the reflectance due to high losses. Furthermore, different refractive indices of the encapsulant material and air manifest themselves in the pulse delay map of THz-TDS data (Fig. 27 e, f). This delay is increased for the part of the sample immersed into

encapsulating material due to higher refractive index in comparison with air-filled void between the glass slide and the silicon solar cell surface [K 3].

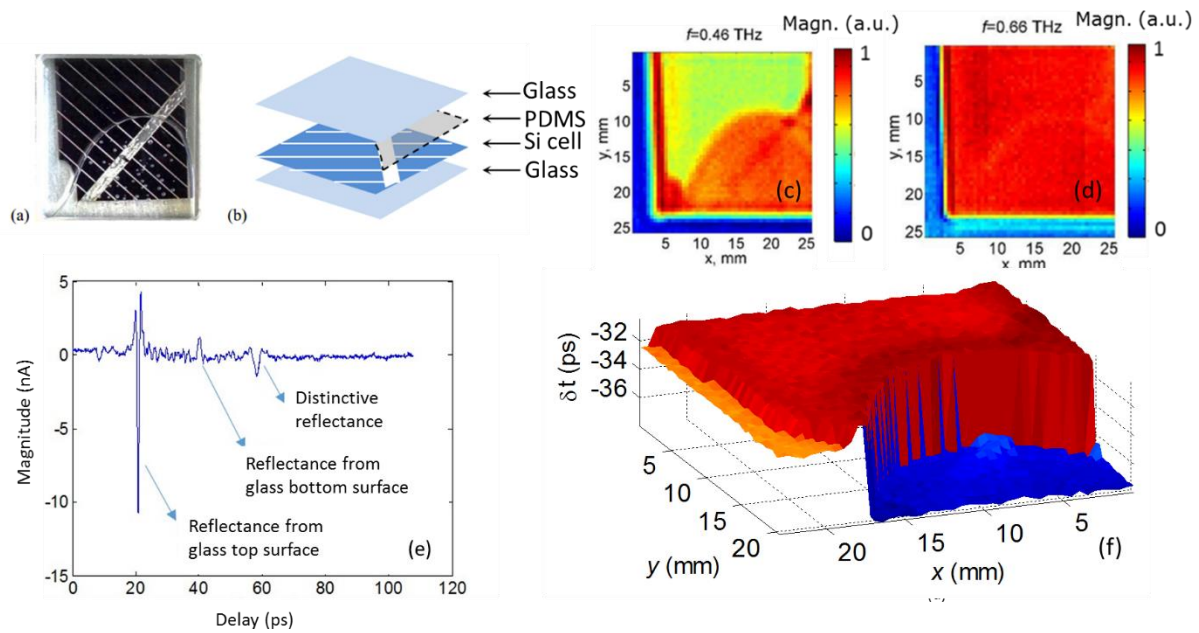


Fig. 27. Photograph and (a) sketch of the layers of the test module structure (b) used for THz imaging. THz reflectance images of the sample recorded at 0.46 THz (c) and 0.66 THz (d). THz waveform recorded at  $x=7.5$  mm,  $y=7.5$  mm dependence of the delay of 3rd pulse on coordinates (e). [K 3]

## 6.4 Chapter summary

It was demonstrated that THz phase imaging data allows a reliable estimation of height differences of bulging tab wires. Also, it was demonstrated, that terahertz radiation can be used to identify defects of encapsulating materials even under the glass layers. In case of anisotropically etched crystalline silicon structures, contactless and therefore easy to integrate into production lines, THz inspection provides reliable means to assess the local average wafer thickness variations and structure depth variations.



## CONCLUSIONS

During the years of doctoral studies bow-tie shaped InGaAs sensors and arrays operating at room temperature have been designed, manufactured and optimized for  $>0.3$  THz frequencies. Diffractive optical components and combined focusing and frequency selective elements for THz frequency range were created. The way to integrate these elements into the sensors arrays in order to increase their sensitivity was proposed. Finally, all these solutions were applied in terahertz imaging systems.

To summarize the work, following conclusions were made:

- 1) The observed reduction of the InGaAs bow-tie detector sensitivity over 1 THz is attributed to the reduction of coupling efficiency due to the antenna properties of the detector contacts. Two different resonance frequencies of two separate parts of antenna explain the scattered experimental points. Finally, it was shown that the “corrected” phenomenological model (with antenna effects inclusion) better matches experimental results at frequencies above 1 THz.
- 2) Previously suggested hot-electron based model explaining the operation principle of bow tie detector was supplemented. It was demonstrated both experimentally and theoretically, that these bow-tie detectors can potentially operate as dual FET self-mixing based detector.
- 3) Bow tie shaped InGaAs detectors are suitable for direct and heterodyne imaging modes. The estimated detectors sensitivity at 0.59 THz is 6 V/W and NEP is 4 nW/ $\sqrt{\text{Hz}}$ . At heterodyne mode NEP – 230 fW/Hz at the minimum detected power of 11  $\mu\text{W}$ . The difference in minimal detectable power between heterodyne and direct modes amounts to about 40 dB.
- 4) In order to avoid cross-talk effects in matrices, period between BT detectors should be at least 120  $\mu\text{m}$  at the frequency range above 0.5 THz. Such chip reduces imaging time 32 times with no loss of resolution comparing with one sensor case.
- 5) A terahertz zone plate and combined zone plate with integrated resonant filters were designed, produced and experimentally characterized. Transmittance of combined zone plates near the resonance peak was found to be similar to that of conventional plates, but they exhibit the added advantage of high selectivity in a frequency scale.

- 6) Bow tie detectivity enhancement of more than one order of magnitude was obtained due to the integrated zone plate on substrate. It was confirmed by measurements at variable angles of incidence radiation and FDTD simulations of the wave propagation.
- 7) THz techniques in contactless way provides reliable means to investigate the local average silicon wafer thickness variations, structure depth variations or module filling layer quality.

## References

- [1] Y. S. Lee, *Principles of terahertz science and technology*, Princ. Terahertz Sci. Technol. (Springer Science & Business Media, 2009).
- [2] J. F. Federici, B. Schulkin, F. Huang, D. Gary, R. Barat, F. Oliveira, ir D. Zimdars, THz imaging and sensing for security applications—explosives, weapons and drugs, *Semicond. Sci. Technol.* **20**(7), S266–S280 (IOP Publishing, 2005).
- [3] F. Wahaiia, G. Valusis, L. M. Bernardo, A. Almeida, J. A. Moreira, P. C. Lopes, J. Macutkevic, I. Kasalynas, D. Seliuta, et al., Detection of colon cancer by terahertz techniques, *J. Mol. Struct.* **1006**(1-3), 77–82 (2011).
- [4] P. H. Siegel, Terahertz technology, *IEEE Trans. Microw. Theory Tech.* **50**(3), 910–928 (2002).
- [5] A. W. Lee ir Q. Hu, Real-time, continuous-wave terahertz imaging by use of a microbolometer focal-plane array, *Opt. Lett.* **30**(19), 2563 (Optical Society of America, 2005).
- [6] J. Trontelj, G. Valušis, R. Venckevičius, I. Kašalynas, A. Sešek, ir A. Švigelj, A high performance room temperature THz sensor, *SPIE Opt. Eng. + Appl.*, (International Society for Optics and Photonics, 2014).
- [7] A. Lisauskas, U. Pfeiffer, E. Öjefors, P. H. Bolivar, D. Glaab, ir H. G. Roskos, Rational design of high-responsivity detectors of terahertz radiation based on distributed self-mixing in silicon field-effect transistors, *J. Appl. Phys.* **105**(11), 114511 (AIP Publishing, 2009).
- [8] A. Sužiedelis, J. Gradauskas, S. Ašmontas, G. Valušis, ir H. G. Roskos, Giga- and terahertz frequency band detector based on an asymmetrically necked n-n[<sup>+</sup>]-GaAs planar structure, *J. Appl. Phys.* **93**(5), 3034 (AIP Publishing, 2003).
- [9] W. Melitz, J. Shen, S. Lee, J. S. Lee, A. C. Kummel, R. Droopad, ir E. T. Yu, Scanning tunneling spectroscopy and Kelvin probe force microscopy investigation of Fermi energy level pinning mechanism on InAs and InGaAs clean surfaces, *J. Appl. Phys.* **108**(2), 023711–023711 – 7 (2010).
- [10] P. H. Siegel ir R. J. Dengler, Terahertz heterodyne imaging part I: Introduction and Techniques, *Int. J. Infrared Millimeter Waves* **27**(4), 465–480 (2007).
- [11] M. Tonouchi, Cutting-edge terahertz technology, *Nat. Photonics* **1**(2), 97–105 (2007).
- [12] C. am Weg, W. von Spiegel, R. Henneberger, R. Zimmermann, T. Loeffler, ir H. G. Roskos, Fast Active THz Cameras with Ranging Capabilities, *J. Infrared, Millimeter, Terahertz Waves* (2009).
- [13] A. Juozapavičius, L. Ardaravičius, A. Sužiedelis, A. Kozi, J. Gradauskas, J. Kundrotas, D. Seliuta, E. Širmulis, S. Ašmontas, et al., Microwave sensor based on modulation-doped GaAs/AlGaAs structure, *Semicond. Sci. Technol.* **19**(4), S436–S439 (2004).
- [14] D. Seliuta, E. Širmulis, V. Tamošiūnas, S. Balakauskas, S. Ašmontas, A. Sužiedelis, J. Gradauskas, G. Valušis, A. Lisauskas, et al., Detection of terahertz/sub-terahertz radiation by asymmetrically-shaped 2DEG layers, *Electron. Lett.* **40**(10), 631 (IET Digital Library, 2004).
- [15] D. Seliuta, I. Kašalynas, V. Tamošiūnas, S. Balakauskas, Z. Martūnas, S. Ašmontas,

- G. Valušis, A. Lisauskas, H. G. Roskos, et al., Silicon lens-coupled bow-tie InGaAs-based broadband terahertz sensor operating at room temperature, *Electron. Lett.* **42**(14), 825 (IET Digital Library, 2006).
- [16] I. Kašalynas, D. Seliuta, R. Simniškis, V. Tamošiūnas, K. Köhler, ir G. Valušis, Terahertz imaging with bow-tie InGaAs-based diode with broken symmetry, *Electron. Lett.* **45**(16), 833 (2009).
- [17] I. Kašalynas, R. Venckevičius, D. Seliuta, I. Grigelionis, ir G. Valušis, InGaAs-based bow-tie diode for spectroscopic terahertz imaging, *J. Appl. Phys.* **110**(11), 114505 (AIP Publishing, 2011).
- [18] A. Taflove ir S. C. Hagness, *Computational Electrodynamics: The Finite-Difference Time-Domain Method*, 3-asis leid. (Artech house, 2005).
- [19] W. Melitz, J. Shen, A. C. Kummel, ir S. Lee, Kelvin probe force microscopy and its application, *Surf. Sci. Rep.* **66**(1), 1–27 (2011).
- [20] Synopsys TCAD, <<http://www.synopsys.com/tools/tcad/Pages/default.aspx>> (7 balandžio 2016).
- [21] J. W. Wu, C. Y. Chang, K. C. Lin, E. Y. Chang, J. S. Chen, ir C. T. Lee, The thermal stability of ohmic contact to n-type InGaAs layer, *J. Electron. Mater.* **24**(2), 79–82 (1995).
- [22] J. Marczewski, W. Knap, D. Tomaszewski, M. Zaborowski, ir P. Zagrajek, Silicon junctionless field effect transistors as room temperature terahertz detectors, *J. Appl. Phys.* **118**(10) (2015).
- [23] A. Lisauskas, D. Glaab, H. G. Roskos, E. Oejefors, ir U. R. Pfeiffer, <title>Terahertz imaging with Si MOSFET focal-plane arrays</title>, *SPIE OPTO Integr. Optoelectron. Devices*, K. J. Linden, L. P. Sadwick, ir C. M. O’Sullivan, Sud., (International Society for Optics and Photonics, 2009).
- [24] B. Voisiat, A. Bičiūnas, I. Kašalynas, ir G. Račiukaitis, Band-pass filters for THz spectral range fabricated by laser ablation, *Appl. Phys. A* **104**(3), 953–958 (2011).
- [25] Reinventing stringers : pv-magazine, <[http://www.pv-magazine.com/archive/articles/beitrag/reinventing-stringers-\\_100003049/329/](http://www.pv-magazine.com/archive/articles/beitrag/reinventing-stringers-_100003049/329/)> (2 gruodžio 2015).
- [26] W. Withayachumnankul ir M. Naftaly, Fundamentals of Measurement in Terahertz Time-Domain Spectroscopy, *J. Infrared, Millimeter, Terahertz Waves* **35**(8), 610–637 (2013).
- [27] T-SPEC series real-time terahertz spectrometer | Ekspla, <<http://www.ekspla.com/product/t-spec-series-real-time-terahertz-spectrometer>> (2 gruodžio 2015).
- [28] BYD to bet on dual-glass modules: pv-magazine, <[http://www.pv-magazine.com/news/details/beitrag/byd-to-bet-on-dual-glass-modules\\_100018110/](http://www.pv-magazine.com/news/details/beitrag/byd-to-bet-on-dual-glass-modules_100018110/)> (5 gruodžio 2015).

## List of publications

- [IP 1] L. Minkevičius, V. Tamošiūnas, K. Madeikis, B. Voisiat, I. Kašalynas, ir G. Valušis, On-chip integration of laser-ablated zone plates for detection enhancement of InGaAs bow-tie terahertz detectors, *Electron. Lett.* **50**(19), 1367–1369 (2014). *Article was selected by Editors as a featured article in front of issue.*
- [IP 2] L. Minkevičius, K. Madeikis, B. Voisiat, I. Kašalynas, R. Venckevičius, G. Račiukaitis, V. Tamošiūnas, ir G. Valušis, Focusing Performance of Terahertz Zone Plates with Integrated Cross-shape Apertures, *J. Infrared, Millimeter, Terahertz Waves* **35**(9), 699–702 (2014).
- [IP 3] L. Minkevičius, S. Balakauskas, M. Šoliūnas, R. Suzanovičienė, J. Uzėla, G. Molis, R. Juškėnas, A. Selskis, G. Niaura, G. Valušis, ir V. Tamošiūnas, Far infrared spectroscopy and imaging of Cu(In,Ga)Se<sub>2</sub> layers, *Lith. J. Phys.* **53**(4), 219–226 (2013).
- [IP 4] L. Minkevičius, B. Voisiat, A. Mekys, R. Venckevičius, I. Kašalynas, D. Seliuta, G. Valušis, G. Račiukaitis, ir V. Tamošiūnas, Terahertz zone plates with integrated laser-ablated bandpass filters, *Electron. Lett.* **49**(1), 49–50 (2013).
- [IP 5] L. Minkevičius, R. Suzanovičienė, S. Balakauskas, G. Molis, A. Krotkus, G. Valušis, ir V. Tamošiūnas, Detection of tab wire soldering defects on silicon solar cells using terahertz time-domain spectroscopy, *Electron. Lett.* **48**(15), 932 (2012).
- [IP 6] L. Minkevičius, V. Tamošiūnas, I. Kašalynas, D. Seliuta, G. Valušis, A. Lisauskas, S. Boppel, H. G. Roskos, ir K. Köhler, Terahertz heterodyne imaging with InGaAs-based bow-tie diodes, *Appl. Phys. Lett.* **99**(13), 1–3 (2011). *This article was chosen as a front-cover of Appl. Phys. Lett.* **99**(13).
- [IP 7] L. Minkevičius, I. Kašalynas, D. Seliuta, V. Tamošiūnas, ir G. Valušis, Frequency-dependent properties of InGaAs bow-tie detectors in terahertz range, *Lith. J. Phys.* **50**(2), 173–180 (2010).

## List of prepared publications

- [PS 1] L. Minkevičius, V. Tamošiūnas, M. Kojelis, E. Žąsinas, V. Bukauskas, A. Šetkus, I. Kašalynas and G. Valušis, „Influence of field effect on the performance of InGaAs-based terahertz radiation detectors“, <http://arxiv.org/abs/1605.00828v1>

## Presentations at the conferences (underlined L. M. – presented personally)

- [K 1] L. Minkevičius, K. Madeikis, B. Voisiat, V. Tamošiūnas, G. Valušis, G. Račiukaitis, ir I. Kašalynas, Compact diffractive optical components for terahertz beam manipulation, 2015 40th Int. Conf. Infrared, Millimeter, Terahertz waves, (IEEE, 2015).
- [K 2] L. Minkevičius, V. Tamošiūnas, I. Kašalynas, R. Venckevičius, K. Madeikis, B. Voisiat, D. Seliuta, G. Račiukaitis, ir G. Valušis, On-chip integration solutions of compact optics and detectors in room-temperature terahertz imaging systems, *SPIE Opt. Eng. + Appl.*, M. Razeghi, A. N. Baranov, J. M. Zavada, ir D. Pavlidis, Sud., (International Society for Optics and Photonics, 2015).
- [K 3] V. Tamošiūnas, L. Minkevičius, A. Vaitkūnas, A. Urbanowicz, A. Maneikis, A. Šetkus, ir G. Valušis, Characterization of Silicon Solar Cells and Module Materials Using Terahertz Radiation, *Energy Procedia* **77**, (2015).
- [K 4] S. Pralgauskaite, J. Matukas, A. Lisauskas, V. Palenskis, I. Kašalynas, L. Minkevičius, D. Seliuta, ir G. Valušis, Low frequency noise characteristics of bow-tie THz detectors based on InGaAs, 2015 Int. Conf. Noise Fluctuations, (IEEE, 2015).
- [K 5] L. Minkevičius, V. Tamošiūnas, I. Kašalynas, B. Voisiat, ir G. Valušis, Terahercinis jutiklis su integruota difrakcine optika, 41-oji Liet. Nac. Fiz. Konf. programa ir pranešimų tezės, (Vilnius, Lietuva, 2015).
- [K 6] G. Valušis, I. Kašalynas, D. Seliuta, R. Venckevičius, L. Minkevičius, V. Tamošiūnas, B. Voisiat, ir G. Račiukaitis, Compact Spectroscopic Terahertz Imaging Systems: Sensors and Optics Design, Ext. Abstr. 3th Int. Symp. Microwave/THz Sci. Appl., (Okinawa, Japan, 2015).
- [K 7] I. Kašalynas, G. Valušis, R. Venckevičius, L. Minkevičius, ir M. Vinciūnas, Compact Spectroscopic Terahertz Imaging Systems for detection of Explosives and CBRN, NATO Adv. Res. Work. THz Diagnostics CBRN Eff. Detect. Explos. CBRN, (Izmir, Turkey, 2015).
- [K 8] G. Valušis, L. Minkevičius, V. Tamošiūnas, I. Kašalynas, R. Venckevičius, K. Madeikis, B. Voisiat, D. Seliuta, ir G. Račiukaitis, Compact optics and detectors for room temperature terahertz imaging

- systems, 51 th Int. Conf. Microelectron. Devices Mater. Work. Terahertz Microw. Syst., (Bled, Slovenia, 2015).
- [K 9] S. Pralgauskaitė, R. Venckevičius, J. Matukas, V. Palenskis, K. Mockus, I. Kašalynas, L. Minkevičius, D. Seliuta, ir G. Valušis, GaAs/AlGaAs supergardių, skirtų terahercinės spinduliuotės detekcijai, žemadažnių triukšmų charakteristikos, 41-oji Liet. Nac. Fiz. Konf. programa ir pranešimų tezės, birželio 17-19 d., (Vilnius, Lietuva, 2015).
- [K 10] L. Minkevičius, V. Tamošiūnas, K. Madeikis, R. Venckevičius, B. Voisiat, I. Kašalynas, ir G. Valušis, Kompaktinės difrakcinės optikos sprendimai terahercinės spinduliuotės fokusavimui, 4-oji doktorantų ir Jaun. Moksl. Konf. spalio 28-29 d., (Vilnius, Lietuva, 2014).
- [K 11] L. Minkevičius, R. Venckevičius, D. Seliuta, I. Kašalynas, G. Valušis, M. Bauer, S. Boppel, A. Lisauskas, V. Krozer, et al., Performance comparison of the terahertz bow-tie-antenna and folded dipole-antenna-coupled AlGaIn/GaN HEMT detectors at frequency 1.43 THz and beyond, international Work. Nitride Semicond. rugpjūčio 24-29, (Wroclaw, Poland, 2014).
- [K 12] I. Kašalynas, L. Minkevičius, R. Venckevičius, D. Seliuta, ir G. Valušis, Multispectra terahertz imaging with antenna-coupled microbolometers, transistors, and bow-tied diodes, Int. Conf. Semicond. Mid-IR Mater. Opt. vasario 26 - kovo 1, (Marburg, Germany, 2014).
- [K 13] I. Kašalynas, L. Minkevičius, R. Venckevičius, D. Seliuta, ir G. Valušis, Multispectral terahertz imaging using compact room temperature operating sensors, GDR-I GDR Work. „Semiconductor sources Detect. THz radiation“, gruodžio 9 - 11 d., (Montpellier, France, 2013).
- [K 14] L. Minkevičius, R. Suzanovičienė, A. Urbanowicz, A. Krotkus, A. Šetkus, ir V. Tamošiūnas, Characterization of encapsulated solar cells by terahertz techniques, 28th Eur. Photovolt. Sol. Energy Conf. Exhib. rugsėjo 30 - spalio 4 d., (Paris, France, 2013).
- [K 15] L. Minkevičius, K. Madeikis, V. Tamošiūnas, D. Seliuta, I. Kašalynas, R. Venckevičius, A. Lisauskas, S. Boppel, H. G. Roskos, G. Valušis, Compact terahertz imaging using antenna coupled bow-tie diodes via direct and heterodyne schemes, Proc. Int. THz Conf. rugsėjo 9 - 10 d., (Villach, Austria, 2013).
- [K 16] S. Boppel, A. Lisauskas, M. Bauer, M. Mundt, V. Krozer, R. Venckevičius, L. Minkevičius, I. Kašalynas, D. Seliuta, G. Valušis, H. G. Roskos, Terahertz detection and mixing with silicon field-effect transistors, Abstr. 15th Int. Symp. Ultrafast Phenom. Semicond. rugpjūčio 25 - 28 d., (Vilnius, Lietuva, 2013).
- [K 17] L. Minkevičius, K. Madeikis, B. Voisiat, A. Mekys, G. Valušis, ir V. Tamošiūnas, Terahercinių zoninių plokštelių su integruotais rezonansiniais filtrais savybių tyrimas, 40-oji Liet. Nac. Fiz. Konf. programa ir pranešimų tezės, birželio 10-12 d, (Vilniaus universiteto leidykla., Vilnius, Lietuva, 2013).
- [K 18] L. Minkevičius, R. Suzanovičienė, S. Balakauskas, M. Šoliūnas, A. Urbanowicz, A. Krotkus, A. Šetkus, ir V. Tamošiūnas, Terahercų dažnių vaizdinimo sistemų taikymas saulės elementų tyrimams, 40-oji Liet. Nac. Fiz. Konf. programa ir pranešimų tezės, birželio 10-12 d, (Vilnius, Lietuva, 2013).
- [K 19] S. Pralgauskaitė, J. Matukas, V. Palenskis, M. Ragauskas, I. Kašalynas, L. Minkevičius, D. Seliuta, ir G. Valušis, Peteliškės tipo InGaAs diodų – terahercinės spinduliuotės detektorių, triukšminių charakteristikų analizė, 40-oji Liet. Nac. Fiz. Konf. programa ir pranešimų tezės, birželio 10-12 d, (Vilnius, Lietuva, 2013).
- [K 20] L. Minkevičius ir V. Tamošiūnas, Zoninių plokštelių įkomponavimo į asimetrinius InGaAs THz detektorius modeliavimas, 3-oji Fiz. ir Technol. Moksl. Cent. doktorantų ir Jaun. Moksl. Konf. rugsėjo 25-26 d., (Vilnius, Lietuva, 2012).
- [K 21] L. Minkevičius, K. Madeikis, I. Kašalynas, R. Venckevičius, D. Seliuta, V. Tamošiūnas, ir G. Valušis, Discrete spectrum terahertz imaging using bow-tie diodes: optimized antenna designs and arrays, SPIE Opt. Eng. + Appl., M. Razežhī, A. N. Baranov, ir J. M. Zavada, Sud., (International Society for Optics and Photonics, 2013).
- [K 22] L. Minkevičius, R. Suzanovičienė, G. Molis, A. Krotkus, S. Balakauskas, R. Venckevičius, I. Kašalynas, I. Šimkienė, G. Valušis, et al., Terahertz techniques for solar cell imaging, Phys. Semicond. Proc. 31st Int. Conf. Phys. Semicond. 2012 **1566**(1), (AIP Publishing, 2013).
- [K 23] L. Minkevičius, K. Madeikis, B. Voisiat, A. Mekys, R. Venckevičius, I. Kašalynas, G. Račiukaitis, G. Valušis, ir V. Tamošiūnas, Study of terahertz zone plates with integrated cross-shape apertures, 2013 38th Int. Conf. Infrared, Millimeter, Terahertz Waves (IRMMW-THz), rugsėjo 1 - 6 d., (IEEE, Mainz, Germany, 2013).
- [K 24] L. Minkevičius, A. Urbanowicz, A. Krotkus, A. Šetkus, ir V. Tamosiunas, Characterization of encapsulation and metal interconnects of solar cells by terahertz techniques, 2013 38th Int. Conf. Infrared, Millimeter, Terahertz Waves (IRMMW-THz), rugsėjo 1 - 6 d., (IEEE, Mainz, Germany, 2013).

- [K 25] M. Ragauskas, V. Palenskis, J. Matukas, S. Pralgauskaitė, L. Minkevičius, I. Kašalynas, D. Seliuta ir G. Valušis, Low frequency noise characteristics of InGaAs bow-tie diodes for terahertz detection, 2013 22nd Int. Conf. Noise Fluctuations, (IEEE, 2013).
- [K 26] L. Minkevičius ir V. Tamošiūnas, Zoninių plokštelių įkomponavimo į asimetrinius InGaAs THz detektorius modeliavimas, 3-oji Fiz. ir Technol. Moksl. Cent. doktorantų ir Jaun. Moksl. Konf. rugsėjo 25-26 d., (Vilnius, Lietuva, 2012).
- [K 27] L. Minkevičius, R. Suzanovičienė, G. Molis, A. Krotkus, S. Balakauskas, R. Venckevičius, I. Kašalynas, I. Šimkienė, G. Valušis, V. Tamošiūnas, Solar cell imaging and characterization by terahertz techniques, 27th Eur. Photovolt. Sol. Energy Conf. Exhib. rugsėjo 24 - 28 d., (Frankfurt, Germany, 2012).
- [K 28] L. Minkevičius ir V. Tamošiūnas, Simulation and investigation of zone plates integration into InGaAs bow-tie diodes, AvH Work. „Advanced Solut. Terahertz Technol. liepos 13 - 16 d., (Riezlern, Austria, 2012).
- [K 29] L. Minkevičius, M. Ragauskas, J. Matukas, V. Palenskis, S. Pralgauskaitė, D. Seliuta, I. Kašalynas ir G. Valušis, InGaAs bow-tie diodes for terahertz imaging: low frequency noise characterisation, SPIE Opt. Eng. + Appl., M. Ramezani, A. N. Baranov, H. O. Everitt, J. M. Zavada, ir T. Manzur, Sud., (International Society for Optics and Photonics, 2012).
- [K 30] L. Minkevičius, R. Suzanovičienė, G. Molis, A. Krotkus, S. Balakauskas, R. Venckevičius, I. Kašalynas, D. Seliuta, G. Valušis, V. Tamošiūnas, Solar cell imaging and characterization by terahertz techniques, SPIE Opt. Eng. + Appl., M. Ramezani, A. N. Baranov, H. O. Everitt, J. M. Zavada, ir T. Manzur, Sud., (International Society for Optics and Photonics, 2012).
- [K 31] G. Valušis, L. Minkevičius, I. Kašalynas, R. Venckevičius, D. Seliuta, V. Tamošiūnas, A. Lisauskas, S. Boppel, H. G. Roskos, et al., Heterodyne and spectroscopic room temperature terahertz imaging using InGaAs bow-tie diodes, 2012 19th Int. Conf. Microwaves, Radar Wirel. Commun., (IEEE, 2012).
- [K 32] L. Minkevičius, I. Kašalynas, V. Tamošiūnas, D. Seliuta, G. Valušis, A. Lisauskas, S. Boppel, H. G. Roskos, ir K. Köhler, Terahertz heterodyne detection and imaging with the InGaAs bow-tie diode, 2011 Int. Conf. Infrared, Millimeter, Terahertz Waves, (IEEE, 2011).
- [K 33] I. Kašalynas, R. Venckevičius, L. Minkevičius, V. Tamošiūnas, D. Seliuta, G. Valušis, A. Lisauskas, S. Boppel, H. G. Roskos, K. Köhler, Properties of the InGaAs bow-tie diode arrays for room temperature terahertz detection, 2011 Int. Conf. Infrared, Millimeter, Terahertz Waves, (IEEE, 2011).
- [K 34] A. Lisauskas, S. Boppel, V. Krozer, H. G. Roskos, L. Minkevičius, D. Seliuta, I. Kašalynas, V. Tamošiūnas, G. Valušis, Terahertz detectors for multipixel coherent imaging, 1st Int. Symp. Terahertz Nanosci., lapkričio 24 - 29 d., (Osaka, Japan, 2011).
- [K 35] A. Lisauskas, S. Boppel, V. Palenskis, J. Matukas, S. Pralgauskaitė, L. Minkevičius, G. Valušis, ir H. G. Roskos, Silicio CMOS detektorių atsako į THz spinduliuotę ir jų žemadažnių triukšmų tyrimai, 39-oji Liet. Nac. Fiz. Konf. spalio 6-8 d., (Vilnius, Lietuva, 2011).
- [K 36] L. Minkevičius, I. Kašalynas, V. Tamošiūnas, D. Seliuta, G. Valušis, A. Lisauskas, S. Boppel, H. G. Roskos, K. Köhler, Heterodininis terahercinis vaizdinimas kambario temperatūroje naudojant InGaAs struktūrinės asimetrijos diodą, 39-oji Liet. Nac. Fiz. Konf. spalio 6 - 8 d., (Vilnius, Lietuva, 2011).

## Curriculum Vitae

<b>Name, Surname:</b>	Linus Minkevičius
<b>Date of birth:</b>	1986 05 21
<b>Place of birth:</b>	Kaunas, Lietuva
<b>Phone and email</b>	+3705 2312418, linas.minkevicius@ftmc.lt
<b>Education:</b>	<p>Date: 2016 Doctoral studies Institution: Center for Physical Science and Technology</p> <p>Date: 2011 Degree: Master degree (Magna cum laude diploma) in material science and semiconductor physics Institution: Vilnius university, Faculty of physics</p> <p>Date: 2009 Degree: Bachelor degree in Applied Physics Institution: Vilnius university, Faculty of physics</p> <p>Date: 2005 Degree: secondary education Institution: Jonas Jablonskis gymnasium</p>
<b>Scientific experience:</b>	<p>Date: since 2008 up to now; Position: engineer, junior-researcher; Institution: Center for Physical Sciences and Technology;</p> <p>Date: since 2012 up to now; Position: assistant Institution: Vilnius university, faculty of physics;</p>
<b>Internship:</b>	<p>2010 07 01 – 09 30 at Physikalisches institute, the Johann Wolfgang Goethe universität, Germany.</p> <p>2013 10 13 – 10 20 at Physikalisches institute, the Johann Wolfgang Goethe universität, Germany.</p>
<b>Specialization:</b>	Standard laser and UV photolithography. Most of know-how relating to THz imaging systems and detectors technology I have acquired during practice in and participating in projects, supported by the Research Council of Lithuania, during 2010 – 2014. Since 2008 I have experience in electrodynamic simulation using the finite difference time domain method, which is used to develop an antenna design of THz detectors, compact diffractive focusing elements and THz filters.